THE SPITZER HIGH REDSHIFT RADIO GALAXY SURVEY

Carlos De Breuck[1], Nick Seymour[2], Daniel Stern[3], S. P. Willner[4], P. R. M. Eisenhardt[3], G. G. Fazio[4], Audrey Galametz[1,3], Mark Lacy[5], Alessandro Rettura[6], Brigitte Rocca-Volmerange[7,8] & Joël Vernet[1]

ABSTRACT

We present results from a comprehensive imaging survey of 70 radio galaxies at redshifts $1 < z < 5.2$ using all three cameras onboard the *Spitzer Space Telescope*. The resulting spectral energy distributions unambiguously show a stellar population in 46 sources and hot dust emission associated with the active nucleus in 59. Using a new *restframe* $S_{3\,\mu m}/S_{1.6\,\mu m}$ versus $S_{5\,\mu m}/S_{3\,\mu m}$ criterion, we identify 42 sources where the restframe $1.6\,\mu m$ emission from the stellar population can be measured. For these radio galaxies, the median stellar mass is high, $2 \times 10^{11}\,M_\odot$, and remarkably constant within the range $1 < z < 3$. At $z > 3$, there is tentative evidence for a factor of two decrease in stellar mass. This suggests that radio galaxies have assembled the bulk of their stellar mass by $z \sim 3$, but confirmation by more detailed decomposition of stellar and AGN emission is needed.

The restframe $500\,MHz$ radio luminosities are only marginally correlated with stellar mass but are strongly correlated with the restframe $5\,\mu m$ hot dust luminosity. This suggests that the radio galaxies have a large range of Eddington ratios. We also present new Very Large Array 4.86 and 8.46 GHz imaging of 14 radio galaxies and find that radio core dominance — an indicator of jet orientation — is strongly correlated with hot dust luminosity. While all of our targets were selected as narrow-lined, type 2 AGNs, this result can be understood in the context of orientation-dependent models if there is a continuous distribution of orientations from obscured type 2 to unobscured type 1 AGNs rather than a clear dichotomy. Finally, four radio galaxies have nearby ($<6''$) companions whose mid-IR colors are suggestive of their being AGNs. This may indicate an association between radio galaxy activity and major mergers.

Subject headings: galaxies: active — galaxies: evolution — galaxies: high-redshift — radio continuum: galaxies

1. INTRODUCTION

Across cosmic time, powerful radio sources are robust beacons of the most massive galaxies in the Universe. At low redshift, this has been known since the first visible counterparts of extragalactic radio sources were shown to be giant elliptical (gE and cD) galaxies (Matthews et al. 1964). In the more distant Universe, indirect evidence for this correlation initially came from a variety of observations, including the near-IR $r^{1/4}$ light profiles of high redshift radio galaxies (HzRGs) at $1 \lesssim z \lesssim 2$ in *Hubble Space Telescope* images (e.g., Pentericci et al. 2000; Zirm et al. 2003) and the tendency for HzRGs to reside in moderately rich (proto-)cluster environments (e.g., Venemans et al. 2007; Galametz et al. 2010). The most direct evidence

comes from the remarkably tight scatter of the observed K-band magnitudes of HzRGs in the Hubble K–z diagram (e.g., Lilly & Longair 1984; Eales et al. 1997; Best et al. 1998; van Breugel et al. 1998; Jarvis et al. 2001; De Breuck et al. 2002; Willott et al. 2003; Rocca-Volmerange et al. 2004; Brookes et al. 2006; Bryant et al. 2009). Assuming that the observed-frame K-band light is dominated by emission from old stellar populations, these studies put HzRGs at the top end of the stellar mass function out to $z = 5.2$. However, this assumption is uncertain due to large band-shifting effects and remaining contributions from the AGN and young stellar populations, which undoubtedly contribute to the observed K-band magnitudes particularly at the highest redshifts where the observed K-band measures rest-frame UV light. As Seymour et al. (2007, hereafter S07) argued in the precursor to this paper, the only solution to minimize these uncertainties is to observe at longer wavelengths with the *Spitzer Space Telescope*. Such observations avoid k-correction effects by consistently observing the same restframe wavelengths where the old stellar population peaks. S07 argued that the restframe H-band luminosity (corrected for non-stellar emission) is the most efficacious band for deriving stellar masses because it corresponds to the minimum in the opacity of the H^- ion (e.g., John 1988) and is associated with a bump in the stellar population SED for almost all stellar populations (e.g., Simpson & Eisenhardt 1999, see S07 for details).

The initial observations for our program, the *Spitzer High-Redshift Radio Galaxy* or SHzRG project, were ob-

[1] European Southern Observatory, Karl Schwarzschild Straße 2, 85748 Garching bei München, Germany; e-mail: cdebreuc@eso.org
[2] Mullard Space Science Laboratory, University College London, Holmbury St Mary, Dorking, Surrey, RH5 6NT, United Kingdom
[3] Jet Propulsion Laboratory, California Institute of Technology, 4800 Oak Grove Drive, Pasadena, CA 91109, USA
[4] Harvard-Smithsonian Center for Astrophysics, 60 Garden Street, Cambridge, MA 02138, USA
[5] National Radio Astronomy Observatory, 520 Edgemont Road, Charlottesville, VA 22903, USA
[6] Department of Physics and Astronomy, University of California, Riverside, CA 92521, USA
[7] Institut d'Astrophysique de Paris, UMR7095 CNRS, Université Pierre et Marie Curie - Paris 6, 98bis boulevard Arago, 75014 Paris, France
[8] Université Paris Sud, Bât 121, 91405 Orsay Cedex, France

tained during *Spitzer* Cycle 1 (Program ID 3329) and involved mid-IR ($\lambda > 3.5\,\mu$m) imaging of 70 HzRGs at $1 < z < 5.2$. S07 reported the sample selection, data processing, and initial results from the full survey. Using imaging from all three instruments on *Spitzer*, S07 decomposed the restframe visible to infrared spectral energy distributions (SEDs) of HzRGs into stellar, AGN, and dust components and determined the contribution of host galaxy stellar emission at restframe H-band to derive stellar masses. S07 found that >60% of restframe H-band light is from stars for the majority of well-studied HzRGs. As expected from unified models of AGNs, the fraction of restframe H-band luminosity due to stars is not correlated with redshift, radio luminosity, or restframe mid-IR ($5\,\mu$m) luminosity. In addition, while the stellar H-band luminosity was not found to vary with stellar fraction, the total H-band luminosity was found to anti-correlate with stellar fraction, as expected if the underlying HzRG hosts comprise a homogeneous population. From a comparison with predicted luminosities from stellar evolution models, S07 found that the HzRG restframe H-band stellar luminosities imply host stellar masses of 10^{11}–$10^{11.5}\,\mathrm{M_\odot}$ for HzRGs, even at the highest redshifts, implying an early formation epoch for these massive galaxies. However, with a large fraction of the sources poorly sampled longward of observed $8\,\mu$m, many of the results of S07 were based on upper limits or on the subset of galaxies with well-sampled SEDs.

In addition to the comprehensive results presented by S07, our SHzRG observations have been used to complement samples of lower redshift radio galaxies (e.g., Haas et al. 2008) and to explore HzRG environments (e.g., Galametz et al. 2009; Doherty et al. 2010; Galametz et al. 2010; Kuiper et al. 2010; Tanaka et al. 2010). The legacy value of the SHzRG program is also seen in the numerous studies of individual HzRGs which have drawn upon the SHzRG data set — e.g., Stern et al. (2006; LBDS 53W091), Villar-Martín et al. (2006; MRC 2104−242), Broderick et al. (2007; PKS 0529−549), Greve et al. (2007; 4C 41.17), Ivison et al. (2008; 4C 60.07), Nesvadba et al. (2009; USS 0828+193), Smith et al. (2010; TXS J1908+7220), and De Breuck et al. (in prep.; 4C 23.56). Follow-up mid-IR spectroscopy of two SHzRG targets (4C 23.56 and 4C 72.26) is also reported by Seymour et al. (2008).

This paper reports the results of a Cycle 4 GTO program (Program ID 40093) to complete the *Spitzer* observations of the SHzRG sample. The observations presented here entail complete six-band 3.6 to 24 μm mid-IR imaging photometry for the entire SHzRG sample using all three instruments on-board *Spitzer*. In addition, new radio observations complete the radio morphological parameters for our sample. Throughout we assume a concordance model of Universe expansion with $\Omega_M = 1 - \Omega_\Lambda = 0.3$, $\Omega_0 = 1$, and $H_0 = 70\ \mathrm{km\,s^{-1}\,Mpc^{-1}}$. Infrared luminosities presented in this paper are of the form $\nu L_\nu / L_\odot$, where $L_\odot = 3.9 \times 10^{26}$ W. Following common practice, radio luminosities at 500 MHz and 3 GHz are expressed as monochromatic luminosity densities.

2. DATA

2.1. *Sample*

The SHzRG sample was described in detail by S07 and is listed in Table 1. In short, we selected 69 powerful radio galaxies[9] from the literature covering a uniform range in both redshift (requiring $z > 1$) and 3 GHz restframe luminosity. In practice, all $z > 3.5$ radio galaxies known in 2004 February were included in our sample. As no low-power radio sources are known as yet at the highest redshifts, we unfortunately are unable to study radio power dependence at $z \gtrsim 3$. At lower redshifts, we preferentially selected those sources with the most supporting data. During Cycle 1, we inadvertently observed MRC 0211−256 ($z = 1.300$) instead of TXS 0211−122 ($z = 2.340$). As the latter is a well-studied radio galaxy with supporting *Hubble Space Telescope* data (van Ojik et al. 1997; Pentericci et al. 2001; Vernet et al. 2001), we have added this source to our sample in Cycle 4, which thus now contains 70 radio galaxies at $1.0 < z < 5.2$.
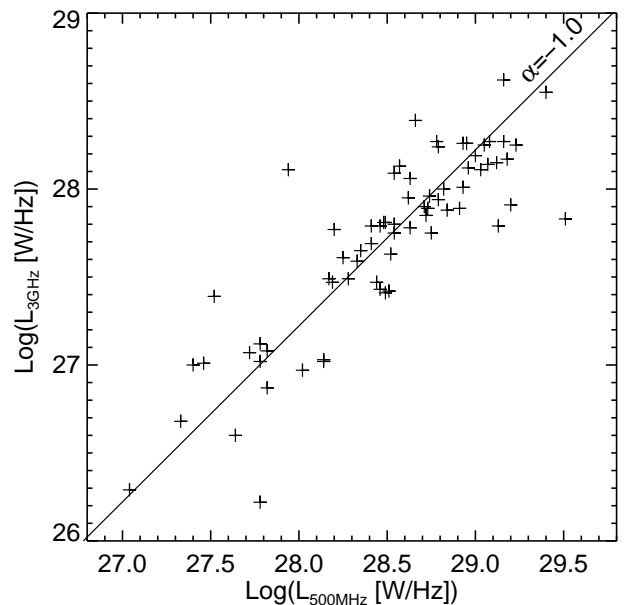
Figure 1. Restframe 3 GHz luminosity plotted against restframe 500 MHz luminosity. The low scatter shows that the contribution by Doppler-boosted radio emission in our sample is nearly always negligible. The solid line shows spectral index $\alpha = -1.0$, typical of the radio galaxies in our sample.

We initially calculated the radio luminosities at a restframe frequency of 3 GHz in order to be able to interpolate between the all-sky, low-frequency (327/352, 365 and 1400 MHz) radio surveys available at the time of our Cycle 1 proposal (Rengelink et al. 1997; Douglas et al. 1996; Condon et al. 1998). Since then, the 74 MHz VLA Low Frequency Survey (VLSS; Cohen et al. 2007) has been completed, covering the entire sky at $\delta > -30°$. Following Miley & De Breuck (2008), we therefore now also calculate restframe 500 MHz luminosities for our sample using the VLSS and the NRAO VLA Sky Survey (NVSS; Condon et al. 1998)[10]. Table 2 lists both the

[9] We define radio galaxies as galaxies (i.e., not type 1 unobscured quasars) with restframe 3 GHz luminosities greater than $10^{26}\,\mathrm{W\,Hz^{-1}}$.

[10] For the few sources not detected in the VLSS, we

500 MHz and 3 GHz restframe radio luminosities. The median flux ratio between the two frequencies is 6.3 for our sample (see Fig. 1), corresponding to a spectral index $\alpha = -1.0$ ($S_\nu \propto \nu^\alpha$). This steeper-than-average spectral index reflects the steep spectrum selection criteria adopted in most of the parent samples from which our targets were drawn.

Figure 2 revisits the radio power–redshift plane used in the definition of our sample. Compared to the 3 GHz luminosity versus redshift plot (bottom panel), there is a slightly larger degeneracy with $L_{500\,\mathrm{MHz}}$ (top panel), particularly at $z > 3.5$ and $z < 2$. Our sample still contains sources with $\log(L_{500\,\mathrm{MHz}}) \sim 28.5$ throughout the redshift range $1 < z < 4.5$ but covers only $\sim$1 dex at a given redshift. As argued by S07, we do not expect Doppler-boosted emission to significantly contribute in our sample, even at restframe 3 GHz. However, in this paper we will use the 500 MHz rather than the 3 GHz luminosities because emission at the lower frequency is expected to be more nearly isotropic (e.g., Blundell et al. 1998).
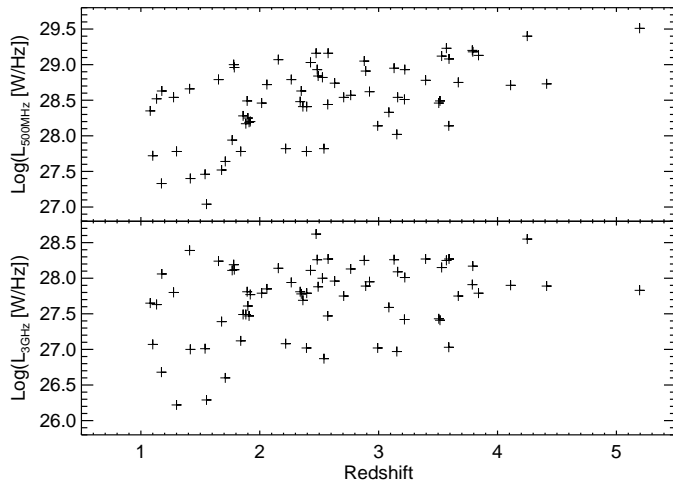
Figure 2. Restframe 500 MHz (top) and 3 GHz (bottom) luminosity plotted against redshift. Redshift and radio power are more degenerate at 500 MHz.

2.2. Spitzer observations

Our Cycle 1 SHzRG observations used a combination of the imaging modes for all three instruments onboard *Spitzer*. We observed (i) all 69 sources from our (initial) sample in all four bands[11] — 3.6, 4.5, 5.8 and 8.0 μm — of the Infrared Array Camera (IRAC; Fazio et al. 2004), (ii) all 46 sources at $z > 2$ using the 16 μm peak-up imaging camera of the InfraRed Spectrograph (IRS; Houck et al. 2004), and (iii) all 26 sources with "low" predicted mid-IR background ($S_{24\,\mu\mathrm{m}} < 20\,\mathrm{MJy\,sr^{-1}}$) in all three bands — 24, 70, and 160 μm — of the Multiband Imaging Photometer for *Spitzer* (MIPS; Rieke et al. 2004). The Cycle 4 program completes the full six-band 3.6 to 24 μm
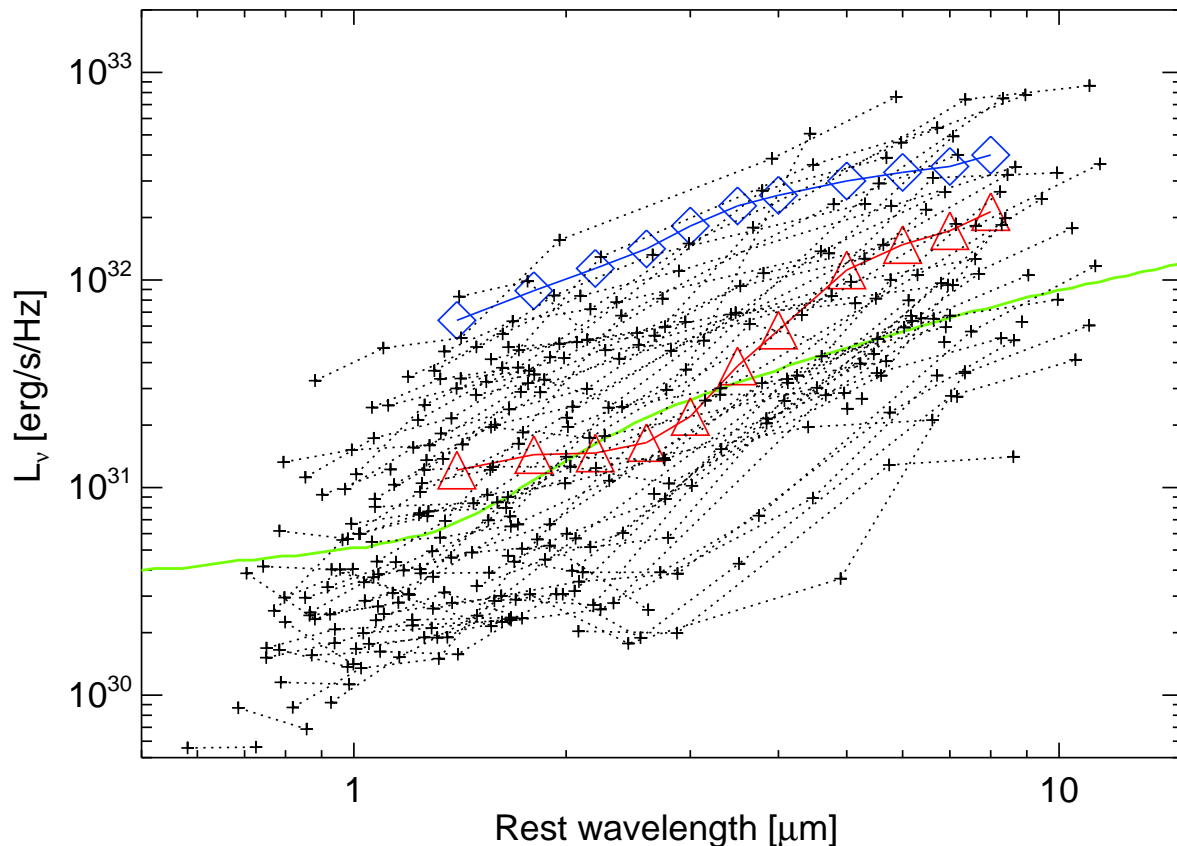
photometry. Table 1 summarizes all *Spitzer* imaging observations of our sample, including those previously published by S07. A handful of sources have significantly deeper *Spitzer* exposures in one or more bands (e.g., deep IRAC observations of 4C 41.17; IRAC and MIPS observations of B2 0902+34). These were obtained by other programs (GO and GTO) and are included here as part of the SHzRG sample. We now describe the Cycle 4 SHzRG program in more detail. Table 3 lists the full six-band photometry for our sample, and Appendix A shows the individual SEDs.

IRAC: We observed only TXS 0211−122 (see §2.1) with IRAC during Cycle 4. The observations were identical to our Cycle 1 program, consisting of four dithered exposures in each of the channels. Data reduction followed the methods described by S07 except that we used IRAC pipeline version 16.1 instead of 13.2. As there are no calibration differences between the pipelines, we did not re-reduce the other IRAC data.

IRS: We observed the 24 $z < 2$ objects using the 16 μm peak-up imaging camera of IRS. During Cycle 1, this observing mode was not officially supported, and we used an experimental double nodding sequence. For the new Cycle 4 observations, we switched to the more efficient peak-up astronomical observing template consisting of five random positions of 30 s ramp duration each. To ensure a fair comparison between our Cycle 1 and Cycle 4 photometry, we re-obtained all our data from the *Spitzer* archive (pipeline version S16.0.0) and re-mosaiced the data with MOPEX. Since the Cycle 1 data consisted of just two exposures, we mosaiced the difference images after subtracting a median to remove the background (including residual images in a few cases). The final images were resampled on a grid with 1″8×1″8 pixels. We extracted the fluxes in circular apertures with a 6-pixel radius and a background subtraction annulus between 6 and 10.7 pixels. We applied an aperture correction of 1.154 to our photometry to obtain total fluxes[12]. The new fluxes listed in Table 3 are on average 50 % higher than the one published by S07 due to the improved calibration.

MIPS: Our Cycle 1 observations gave a low detection rate in the MIPS 70 μm imaging (five out of 24: 21%) and no detections at 160 μm. The 44 HzRGs not observed with MIPS during Cycle 1 were omitted because of the larger predicted background emission ($S_{24\,\mu\mathrm{m}} > 20\,\mathrm{MJy\,sr^{-1}}$, see S07) at their positions. Because of the low detection rate at 70 and 160 μm and the higher expected background emission due to zodiacal and Galactic cirrus emission, an observing request aimed at detecting our complete sample at these wavelength was considered impractical. We therefore decided to concentrate on 24 μm imaging during Cycle 4. To compensate for the higher expected sky background, the new 24 μm observations consisted of two cycles of 30 s exposures each (totaling 28 individual images compared to a single cycle, i.e., 14 images, in our Cycle 1 observations). One radio galaxy, MRC 0156−252, was not observed before the end of the *Spitzer* cryogenic mission. To ensure a fair comparison of flux densities between Cycles 1 and 4, we re-obtained the data from the archive (pipeline version S16.1.0) and mosaiced and derived photometry in the

---

used the 325 MHz Westerbork Northern Sky Survey (WENSS; Rengelink et al. 1997) or the 365 MHz Texas survey (Douglas et al. 1996).

[11] With the exception of 3C 65, which was only observed in the 3.6 and 5.8 μm bands (see S07). As the source is dominated by hot dust emission at $\lambda_{\mathrm{obs}} = 5.8\,\mu\mathrm{m}$, we did not re-observe it at 4.5 and 8.0 μm during Cycle 4

[12] See http://ssc.spitzer.caltech.edu/irs/irsinstrumenthandbook/45/

De Breuck et al.

Figure 3. Restframe luminosity density of the *Spitzer* data in our sample. The red triangles show the average 3CRR radio galaxy SED and the blue diamonds the average quasar SED from Leipski et al. (2010), both based on objects with $1 < z < 1.4$ and normalized to radio flux density. The green solid line is the mean SED of all SDSS (visible color selected, radio quiet) type-1 AGNs from Richards et al. (2006) normalized to 0.08 mJy at 2500 Å.

same fashion as S07. Sources with predicted sky background levels $S_{24\,\mu m} > 40\,\mathrm{MJy,sr^{-1}}$ are affected by strong remaining gradients in the combined images. While such fields are not appropriate to study the environment of the HzRGs (Mayo et al., in prep.), the images can still be used to obtain reliable photometry for the central radio galaxies. The one exception is 5C 7.269, the source with the highest observed background level in our sample ($S_{24\,\mu m} = 65\,\mathrm{MJy,sr^{-1}}$), which saturated the MIPS detector.

2.3. *New radio data*

Of the 70 sources in our SHzRG sample, 49 already had high resolution ($0''5$) radio maps available from the Very Large Array (VLA; Napier et al. 1983) or the Australia Telescope Compact Array (ATCA; Frater Brooks & Whiteoak 1992). Most of these observations are contained in the compendia published by Carilli et al. (1997) and Pentericci et al. (2000). To complete the radio observations for our sample, we observed the remaining 21 sources with the VLA in the A configuration between 2006 February 20 and 2006 March 16 (observing project ID AD520). For consistency, we used the same observational setup as Carilli et al. (1997) and Pentericci et al. (2000); i.e., 10 to 40 min of snapshot observations in C-band (4.86 GHz) and 20 to 80 min in X-band (8.46 GHz). We followed the standard calibration

and imaging reduction steps in the Astronomical Imaging Processing System ($\mathcal{AIPS}$) and the Common Astronomy Software Applications (CASA).

Table 2 summarizes the archival and new radio data for our sample. We classified the radio structures into three classes: S = single component (i.e., spatially unresolved sources); D = double component sources without a core detection; and T = core-detected, resolved sources, which are generally triple component sources with a core and two radio lobes. For all sources, we measured the largest angular size θ (Carilli et al. 1997) of the radio structure. For sources with a core detection, we list the core fraction at a restframe frequency of 20 GHz, CF_{20} (following the definition of Carilli et al. 1997). Appendix B shows contour plots of the new radio data.

3. MID-IR SPECTRAL ENERGY DISTRIBUTIONS

3.1. *Mean HzRG SED*

As our *Spitzer* survey presents the largest collection of mid-IR photometry of targeted, high-redshift type 2 AGNs, we first examine the general trends in their SEDs. Figure 3 shows the restframe infrared luminosity densities from our *Spitzer* photometry. There is a scatter of ~ 2 dex at any given rest wavelength with a notable exception around $\lambda_{\mathrm{rest}} = 1.6\,\mu\mathrm{m}$, where the scatter decreases to 1.5 dex. This wavelength corresponds to the

peak in old stellar populations (e.g., Sawicki 2002), and the decreased scatter suggests that the stellar population dominates the SEDs at this wavelength. The $1.6\,\mu$m peak is most pronounced in the lowest luminosity objects and tends to become less obvious in sources with greater mid-IR luminosity. Almost all the SEDs show a sharp rise at $\lambda_{\rm rest} > 2\,\mu$m due to the onset of hot dust emission at longer wavelengths.

The average radio galaxy SED as derived by Leipski et al. (2010) is a good match to our sample, though the most luminous sources have SEDs compatible with either of the two quasar SEDs shown in Figure 3. The radio galaxy points have a steeper rise between restframe $\sim$2 and $\sim$8 μm than the quasar composites. This indicates that the hottest dust emission is highly extincted or absent in radio galaxies, as suggested by orientation unification models (e.g., Ogle et al. 2006; Cleary et al. 2007; Haas et al. 2008; Leipski et al. 2010). At $\lambda_{\rm rest} < 2\,\mu$m, the radio galaxy SEDs are on average about half as luminous as the quasar composite for a given $\lambda_{\rm rest} = 8\,\mu$m luminosity density. The radio galaxy SEDs at $\lambda_{\rm rest} < 2\,\mu$m are at least as blue as those of the quasars and are consistent with a stellar population rather than hot dust emission. In fact, for many sources a clear dip is seen between the stellar peak at restframe $1.6\,\mu$m and the rising dust emission at longer wavelengths. It therefore seems feasible to derive robust stellar masses from our *Spitzer* photometry, at least for a subset of our sample, though given the large spread in SED shapes, great care needs to be taken to separate stellar and dust emission in each individual galaxy. The next two subsections describe our SED modeling and how well we can separate these components.

3.2. *SED modeling*

We used a slightly updated version of the model described by S07 to fit the *Spitzer* radio galaxy SEDs. For the host galaxy component, we used elliptical galaxy templates calculated from the PÉGASE[13] spectrophotometric model (Fioc & Rocca-Volmerange 1997) with an assumed formation redshift $z_{\rm form}$=10 and a Kroupa (2001) initial mass function. (S07 give further details about the template and the influences of changing the IMF, the formation redshift, and the treatment of extinction and thermally pulsing asymptotic giant branch stars.) Templates for individual galaxies differ only in overall stellar mass and in the amount of passive evolution from $z = 10$ to the individual galaxy redshift. To describe the dust emission, we used a simple model consisting of three pure blackbody components: (i) a $T = 60\,$K component, which was used only for the five sources with $70\,\mu$m detections; (ii) a $T = 250\,$K component[14]; and (iii) a component with $500 < T < 1500\,$K, where the temperature was a free parameter. This model with four free parameters (five for those sources with $70\,\mu$m detections) was fit to our six (or seven) broad-band data points. For sources undetected in the longer wavelength data, we fit a maximum dust emission model through the 3σ upper limit at $\lambda_{\rm obs} = 16\,\mu$m or $24\,\mu$m, whichever is more sensitive, in order to obtain reliable upper lim-

---

[13] http://www.iap.fr/pegase
[14] For 6C 0032+412, we had to modify this to a $T = 650\,$K component, see §4.3.2.

its to the hot dust emission. When the two limits were within 10 % of each other, the maximum dust emission was fitted through both. The contributions from stellar populations at $\lambda_{\rm obs} = 24\,\mu$m are expected to be more than an order of magnitude lower than the depth of our MIPS photometry and can therefore be ignored. Physical dust models with a proper treatment of a clumpy torus, viewing angle geometry, and radiative transfer exist in the literature (e.g., Pier & Krolik 1992; Granato et al. 1997; Nenkova et al. 2002; Elitzur & Shlosman 2006; Fritz et al. 2006; Siebenmorgen & Krügel 2007). However, a detailed analysis using these models would overinterpret our data as the models require mid-IR spectroscopy for a detailed fitting of spectral features. Seymour et al. (2008) presented IRS spectroscopy of two sources from our sample, and further IRS spectroscopy of five sources in our sample will be presented in a future manuscript (J. Rawlings et al. 2011, in prep.). As these data cover only 10% of our sample, here we use only broad-band photometry and restrict our analysis to separating the stellar and hot dust emission in order to determine interpolated restframe luminosities.

Other components besides dust and stars can contribute to the mid-IR emission. Non-thermal synchrotron emission has been detected in *Spitzer*/IRS spectroscopy of several 3CR sources (e.g., Cleary et al. 2007; Leipski et al. 2009). However, this component is only seen in type 1 AGNs dominated by flat radio spectra. Our radio galaxies have much steeper radio spectral indices (see Fig. 1) and have low radio core dominance (see Table 2). Miley & De Breuck (2008) showed the SED of 4C 23.56, which is one of the most core-dominated sources in our sample ($CF_{20} = 14.6\%$), and even for this galaxy, the synchrotron contribution near the peak of the far-IR SED at $\lambda_{\rm rest} = 50\,\mu$m is at least five orders of magnitude lower than the dust emission. We therefore do not consider a synchrotron component in our models.

More important contributions can be expected from mid-IR spectral features such as PAH emission at $7.7\,\mu$m and silicate absorption at $9.7\,\mu$m. Both of these features have been detected in individual galaxies in our sample (Seymour et al. 2008; Leipski et al. 2010). However, our photometric bands are wide, and the equivalent width of PAH emission is low compared to the underlying hot dust continuum emission. We therefore do not expect these lines to have a significant effect on our photometry. The silicate feature may have some discernible effect, but as we cover restframe $9.7\,\mu$m only for $z < 1.5$, at most a small subset of our sample can be affected. Furthermore, the composite radio galaxy template of Haas et al. (2008) implies that neither PAH emission nor silicate absorption is expected to have strong effects on the mid-IR SEDs, and thus neither of them is considered in our modeling.

Finally, the Hα emission line shifts into the IRAC $3.6\,\mu$m band at $z > 3.7$ (e.g., Assef et al. 2010). In at least one of the seven SHzRG sources at $z > 3.7$, TN J1338−1942 at $z = 4.1$, we indeed notice an unusual factor of $\sim$2 increase in the $3.6\,\mu$m photometry compared to the K-band and $4.5\,\mu$m points (see Appendix A). We therefore use IRAC $3.6\,\mu$m photometry at $z > 3.7$ only to verify the consistency of our stellar population but not to fit the SED.

Appendix A shows the SEDs including model fitting of the 70 sources in our sample, ordered by increasing red-
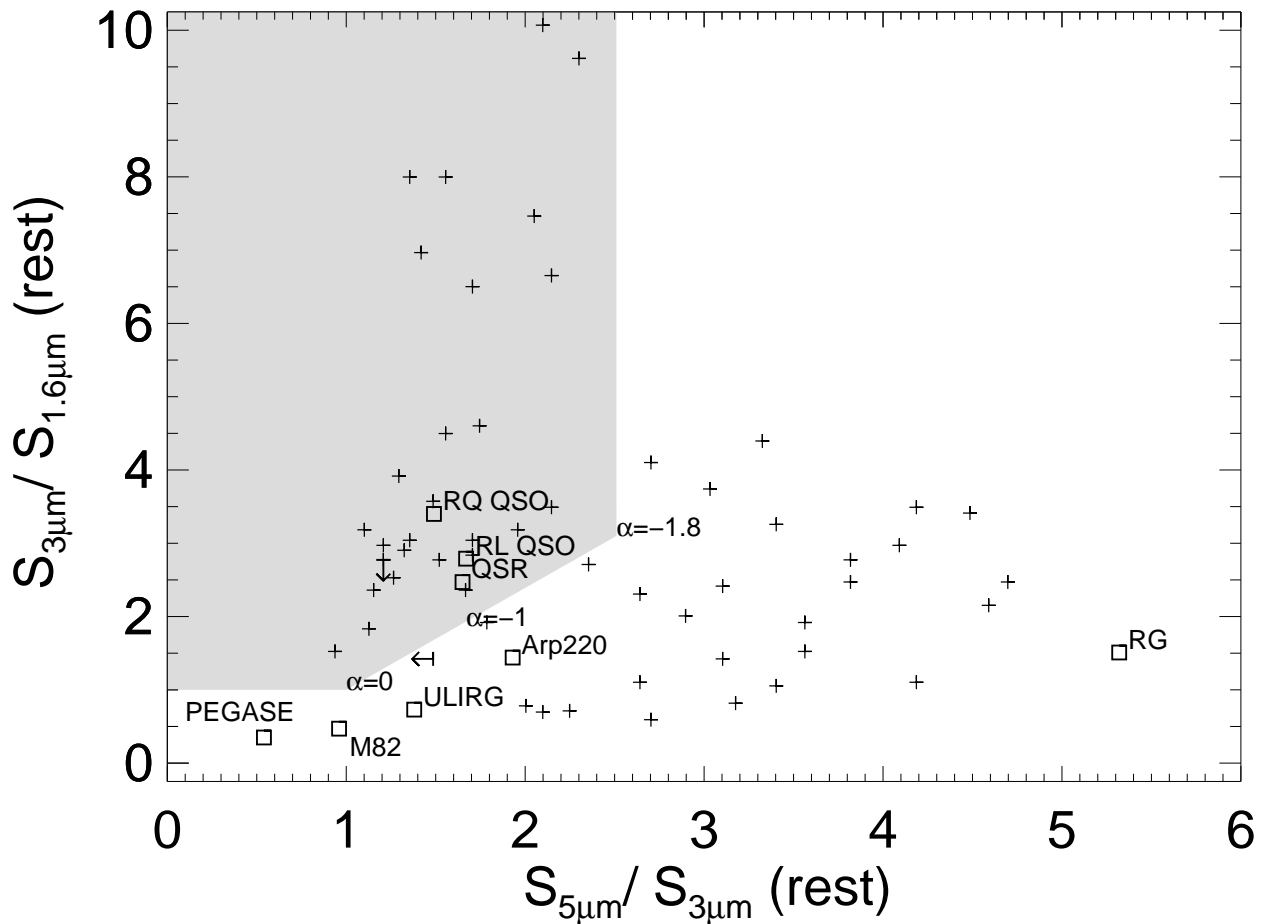
Figure 4. Restframe mid-IR color-color diagram. The shaded area marks the region where $\lambda_{\rm rest} \approx 1.6\,\mu$m is dominated by hot dust rather than stellar emission. The slanted boundary marks the locus of straight power-law SEDs with $-1.8 < \alpha < 0$ as labeled. Open squares mark the locations of two well known objects (M82, Arp 220; Devriendt et al. 1999), the average quasar (QSR) and radio galaxy (RG) SED of Leipski et al. (2010), the radio-loud (RL) and radio-quiet (RQ) QSO composite of Elvis et al. (1994), the ultraluminous infrared galaxy (ULIRG) SED of Rieke et al. (2009), and the PÉGASE galaxy spectrophotometric model described in §3.2.

shift. As already apparent from Fig. 3, the HzRG SEDs are quite diverse. Some galaxies such as 7C 1751+6809 ($z = 1.540$) show a clear stellar contribution recognized by a decline in flux density from restframe $1.6\,\mu$m to longer wavelengths and a distinct hot dust component steeply rising beyond restframe $3\,\mu$m. Other galaxies such as 3C 257 ($z = 2.474$) or PKS 1138−262 ($z = 2.156$) have mid-IR SEDs consistent with a power-law. For such sources, we can only derive upper limits to the mass of the host galaxy stellar population. The SED of TXS J1908+7220 ($z = 3.530$) is dominated by a transmitted quasar continuum (see §4.3.2) and also allows only an upper limit to be derived on the stellar population.

3.3. *Separation of stellar and dust emission*

Spitzer multi-band photometry is a powerful tool to trace the mid-IR emission from AGNs. Various IRAC and MIPS color selection criteria have been designed to identify AGNs (e.g., Ivison et al. 2004; Lacy et al. 2004; Stern et al. 2005; Pope et al. 2008). S07 showed that 71% and 88% of the SHzRG sources fall within the Stern et al. (2005) and Lacy et al. (2004) IRAC color-

color AGN selections, respectively. Because 16 sources in our sample have only upper limits in the pivotal $8\,\mu$m band, the $S_{24\,\mu{\rm m}}/S_{8\,\mu{\rm m}}$ versus $S_{8\,\mu{\rm m}}/S_{4.5\,\mu{\rm m}}$ diagrams of Ivison et al. (2004) and Pope et al. (2008) are not very useful for our sample. These *observed-frame* color-color selection techniques have two major limitations for our purposes: (1) our sample consists, by definition, of type 2 AGNs, so we are not interested in *finding* AGNs but rather in determining the AGN contribution relative to the host galaxy; and (2) our sample covers $1 < z < 5.2$, while these techniques are not uniformly sensitive over this full redshift range (e.g., Assef et al. 2010).

As we have full redshift information for our sample, we set up a new *restframe* color selection criterion to identify those sources with strong dust contributions at restframe $1.6\,\mu$m, where the stellar population peaks. To interpolate the data between our six photometric data points, we used our fitted model (see §3.2). As our bands are wide and often contiguous, the use of this model should not introduce significant interpolation errors as can be seen from the individual SEDs in Appendix A. Haas et al. (2008) introduced a restframe $S_{3\,\mu{\rm m}}/S_{1.6\,\mu{\rm m}}$

versus $S_{5\,\mu m}/S_{8\,\mu m}$ diagram to separate the quasar and radio galaxy SEDs in their 3CR sample at $1 < z < 2.5$. We modified this criterion for use at $z > 2.5$, where MIPS $24\,\mu m$ photometry only covers out to $\lambda_{rest} \lesssim 5\,\mu m$. On the blue end, the data cover the peak of the stellar emission at $\lambda_{rest} \leq 1.6\,\mu m$ for our entire sample. Considering an even bluer λ_{rest} would be possible observationally but would increase the contributions from younger stellar populations (see S07) as well as non-stellar contributions such as scattered quasar emission and nebular emission (see Miley & De Breuck 2008). We also wanted our criterion to pick up a possible minimum in the SEDs longward of the Rayleigh-Jeans fall-off of the stellar emission at $\lambda_{rest} \gtrsim 2\,\mu m$ and the onset of the steeply rising, hot dust continuum. While the stellar peak has a unique shape, the dust continuum slope depends on the temperature and obscuration of the hot dust emission. Moreover, the relative offset between the stellar and hot dust components can vary substantially as discussed in §3.1. We therefore identified $\lambda_{rest} = 3\,\mu m$ as the pivot wavelength for our new criterion. This wavelength is also located centrally between 1.6 and $5\,\mu m$, which minimizes the effect of measurement errors on our photometry. Table 4 lists the monochromatic luminosities at 1.6, 3, and $5\,\mu m$ as derived from our SED fitting. Table 4 also lists the fraction of stellar light at $\lambda_{rest} = 1.6\,\mu m$ and the stellar masses derived following the procedures of S07.

Figure 4 shows the restframe $S_{3\,\mu m}/S_{1.6\,\mu m}$ versus $S_{5\,\mu m}/S_{3\,\mu m}$ color-color diagram for our sample. All AGN-dominated SEDs cluster around $(S_{5\,\mu m}/S_{3\,\mu m}, S_{3\,\mu m}/S_{1.6\,\mu m}) \sim (1.5, 3)$. This corresponds to an SED which is still steepening at $\lambda_{rest} < 3\,\mu m$, indicative of the warm temperature limit of the dust emission with a possible contribution from extinction (e.g., Haas et al. 2008; Leipski et al. 2010). Sources with very red SEDs at $\lambda_{rest} < 3\,\mu m$ (upper left corner in Fig. 4) are therefore likely to be dominated by AGN dust emission. Park et al. (2010) showed that *Spitzer* power law galaxies have 3–$24\,\mu m$ spectral indices $-1.8 < \alpha < 0$ ($S_\nu \propto \nu^\alpha$). We therefore defined the straight power law locus as a boundary in Fig. 4 to separate AGN dust emission and host galaxy (stellar) dominated HzRGs. Sources with $\alpha < -1.8$ are indicative of strong extinction already in the $\lambda_{rest} = 3$–$5\,\mu m$ range and are not expected to have significant remaining dust emission at $1.6\,\mu m$. Sources with $S_{3\,\mu m}/S_{1.6\,\mu m} < 1$ are consistent with stellar populations as confirmed by the positions of the PÉGASE and M82 SED in Fig. 4. Summarized, we defined sources dominated by an AGN at $1.6\,\mu m$ by the criterion:

$$S_{3\,\mu m}/S_{1.6\,\mu m} > 1$$

$$\cap$$

$$S_{3\,\mu m}/S_{1.6\,\mu m} > 1.39 \times S_{5\,\mu m}/S_{3\,\mu m} - 0.39$$

$$\cap$$

$$S_{5\,\mu m}/S_{3\,\mu m} < 2.5$$

Even with our criterion, classification of individual objects is uncertain, especially near the boundaries: (1) measurement errors may shift objects across the boundaries, (2) variations in the interpolation between the bands using the SED model described in §3.2 cause

some uncertainties, and (3) contributions from other non-stellar components such as a transmitted or scattered quasar continuum might require a more complex model for some sources (e.g., TXS J1908+7220, see §4.3.2). For individual sources, a more accurate separation would be possible when using additional supporting data such as IRS spectra or multi-band near-IR and visible imaging. This is beyond the scope of the current paper and would also introduce redshift dependence in the results. We are mainly interested in looking for statistical correlations, and our rest-frame color criterion allows a uniform treatment for all sources within our sample.

For 15 sources in our sample (mostly at $z > 2$), we could obtain only upper limits on the hot dust emission; these were determined from the MIPS $24\,\mu m$ limits only, as our MIPS images are significantly more sensitive than the IRS $16\,\mu m$ imaging. However, the IRS and MIPS photometry is sufficiently sensitive to assure that the IRAC detections are dominated by stellar emission (e.g., TN J1338$-$1942 at $z = 4.1$). In total, we derived reliable stellar masses for 42 HzRGs (see also §4.1). For the remaining 28 sources, we used the same procedure to correct the $\lambda_{rest} = 1.6\,\mu m$ flux from the extrapolated hot dust model and fit the stellar template to the remaining photometry. This procedure does become less reliable: the median $1.6\,\mu m$ stellar fraction of these 28 sources is 0.71 compared to 0.96 for the sources outside the AGN-dominated area (see table 4). While the stellar masses may be close to the real ones (especially for sources near the boundary in Fig. 4), we conservatively treat them as upper limits.

4. RESULTS

Having identified that both stellar mass and AGN-heated dust emission contribute significantly to the near- and mid-IR SEDs of HzRGs, we now examine the correlation between the physical parameters in our sample. In order to properly consider the upper limits in the statistical tests of the significance of correlations, we make use of survival analysis and in particular the generalized Spearman's ρ coefficient (e.g., Isobe et al. 1986). Results are expressed in terms of the probability P of seeing the observed or a higher value of ρ if the null hypothesis that the data are uncorrelated holds. Thus a small value of P indicates a high likelihood that a correlation exists.

4.1. *Stellar masses*

The original motivation of our *Spitzer* survey was to derive accurate stellar masses by consistently observing the same restframe wavelength where the old stellar population peaks, which S07 argued is at restframe H-band. Figure 5 updates the HzRG restframe H-band stellar luminosity density–redshift relation. The only difference from the S07 version is that with full IRS and MIPS photometry, we now have a better handle on the hot dust emission, particularly for sources where previously we obtained only upper limits on the stellar masses (see §3.3). The stellar rest-frame H-band luminosity shows no correlation with redshift ($P = 0.42$).

Figure 6 shows the redshift evolution of the derived stellar masses. We confirm the result of S07 that HzRGs have high stellar masses at every redshift. However, we now find a trend for the $z > 3$ radio galaxies to be slightly
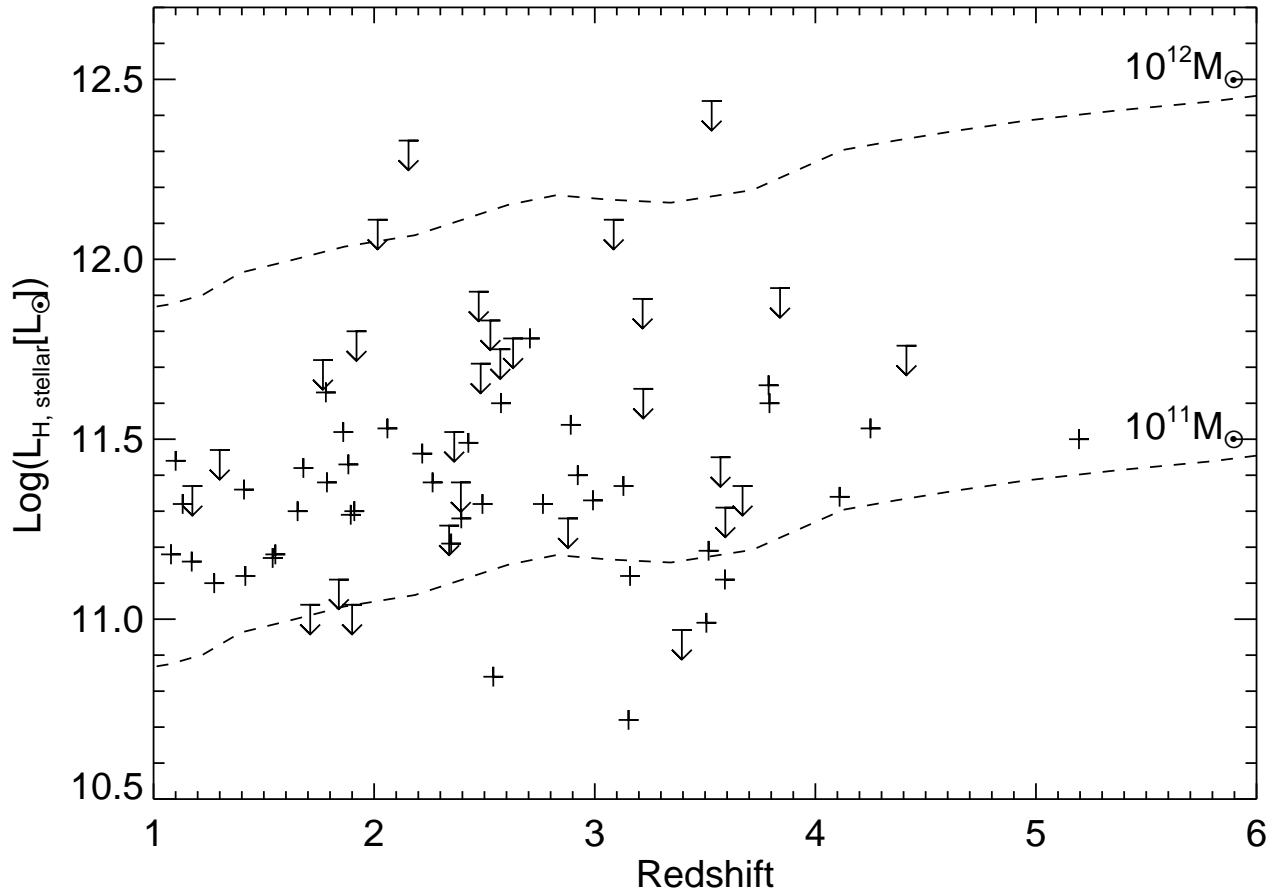
Figure 5. Restframe H-band stellar luminosity versus redshift for the *Spitzer* HzRG sample, derived from the best-fit models to the multi-band photometry. Upper limits indicate radio galaxies where only a maximum fit to the stellar SED was possible. The dashed lines show the luminosities of PÉGASE.2 elliptical galaxy models (Rocca-Volmerange et al. 2004) with $z_{form} = 10$ and masses 10^{11} and $10^{12}\,M_\odot$.

less massive ($P = 0.0044$). The drop in stellar mass becomes apparent only at $z \gtrsim 3$. Considering only the subset of sources at $z < 3$, the correlation becomes insignificant ($P = 0.19$). We caution that the putative mass decrease is based on only 11 reliable stellar mass determinations at $z > 3$, and the decrease in stellar mass is very small: the median stellar mass of $z < 3$ HzRGs is $2.3 \times 10^{11}\,M_\odot$ versus $1.6 \times 10^{11}\,M_\odot$ for $z > 3$. If confirmed, the difference would indicate that radio galaxies are still forming at $z > 3$ but have already assembled the bulk of their stellar mass by $z \sim 3$. This pivotal redshift is consistent with the increase in the submillimeter detection rate of radio galaxies at $z > 3$, where submm flux densities above a few mJy imply extreme star formation rates exceeding $1000\,M_\odot\,yr^{-1}$ (Archibald et al. 2001; Reuland et al. 2004). A more elaborate spectral decomposition would be required to better quantify the reality of this small drop in stellar mass. In particular, rest-frame visible and UV photometry and polarimetry are needed to properly extrapolate the scattered and transmitted AGN contributions. In addition, dust obscuration may affect even restframe near-IR emission in the host galaxy (e.g., Dey et al. 2008). While the bright submm emission in some $z > 3$ radio galaxies suggests they may indeed contain large amounts of dust (though

the submm brightness is most likely dominated by higher star formation rates), we do not expect this dust to cause large obscurations because HzRG extended emission lines, in particular Lyα, are less obscured at $z > 3$ than at $z < 3$ (Villar-Martín et al. 2007).

### 4.1.1. *Dependence of stellar mass on radio luminosity and black hole activity*

Figure 7 revisits the marginal correlation between stellar mass and radio power discussed by S07. Our new plot is more reliable in two ways: (i) it uses the more nearly isotropic 500 MHz rather than the 3 GHz radio luminosity, and (ii) it has more reliable determinations of stellar mass upper limits (see §3.3). Our full data set confirms the result of S07 that radio power and stellar mass are not significantly correlated ($P = 0.26$). The absence of a stronger $M_{stellar}$–$L_{500\,MHz}$ correlation is slightly surprising given previous claims of a correlation between radio power and *observed* K-band magnitude (Eales et al. 1997; Best et al. 1998; Jarvis et al. 2001; De Breuck et al. 2002; Willott et al. 2003). Apart from the difficulty in disentangling redshift and radio luminosity effects in samples affected by a strong Malmquist bias, the correlations with K-band magnitude apparently stem from other components that correlate with radio power such as transmitted and/or scattered quasar light, neb-
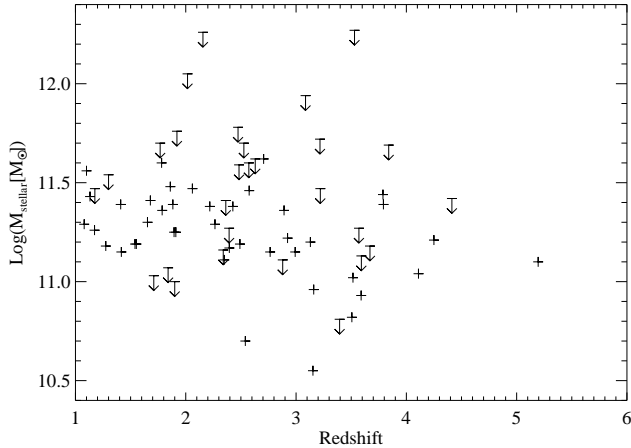
Figure 6. Stellar mass versus redshift for the *Spitzer* HzRG sample. Masses are based on the SED decomposition described in §4 and the PÉGASE.2 models (Rocca-Volmerange et al. 2004).

ular emission (continuum and/or lines), or (in the low-redshift objects) the tail of the hot dust emission.
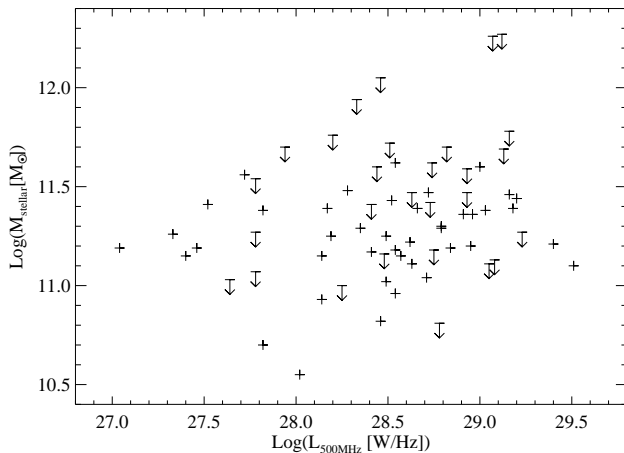
Figure 7. Stellar mass (§4) versus restframe 500 MHz radio luminosity for the *Spitzer* HzRG sample.

The limited radio luminosity range of our sample and the small spread in stellar masses make it difficult to detect any but a strong correlation. However, we can also turn this argument around and suggest that the low stellar mass spread is proof that radio power, stellar mass, or both are not strongly correlated with the accretion properties of the central supermassive black hole (SMBH). The correlation between the mass of the nuclear black hole and the stellar bulge is now well established (Magorrian et al. 1998; Häring & Rix 2004). If this relation also holds for HzRGs, the small range in stellar masses would also imply a small range in black hole masses. Based on spectroscopy of six broad Hα

lines in HzRGs[15], Nesvadba et al. (2010) do indeed find all black hole masses in the range $M_{\rm BH} = 3 \times 10^9$ to $2 \times 10^{10}\,{\rm M}_\odot$, which puts them only slightly offset from the local $M_{\rm BH}$–$M_{\rm bulge}$ relation. While further $M_{\rm BH}$ determinations would be needed to check this trend, it seems likely that HzRGs contain SMBHs with masses similar to those expected.

On the other hand, low frequency radio luminosity is only one of the estimators of the jet kinetic power (Willott et al. 1999; Cattaneo & Best 2009) and hence black hole activity. Comparisons with other measurements, such as the amount of kinetic power needed to create X-ray cavities (Bîrzan et al. 2008, 2010; Cavagnolo et al. 2010), show that there can be an uncertainty of more than an order of magnitude in this determination. Intrinsic spread in the radio luminosity–jet power relation, environmental effects (e.g., density of the medium in which the radio source is expanding), and variations in the Eddington ratios of SMBHs of similar mass may therefore imply that the 500 MHz luminosity does not provide a very reliable measure of the black hole properties, at least not in the limited 2 dex range of the most luminous HzRGs studied by our sample.

4.2. *Mid-IR luminosities*

Before the launch of *Spitzer*, AGN-heated dust emission remained a virtually unexplored component in $z > 1$ radio galaxies, apart from mostly upper limits obtained by the *Infrared Space Observatory* (e.g., Meisenheimer et al. 2001; Andreani et al. 2002; Haas et al. 2004). S07 presented *Spitzer* results regarding the mid-IR luminosities of HzRGs, and Section 3 advances the argument that the $\lambda_{\rm rest} > 3\,\mu{\rm m}$ emission of HzRGs is dominated by hot dust. The complete IRS $16\,\mu{\rm m}$ and MIPS $24\,\mu{\rm m}$ photometry presented herein permit further analysis. Hot dust emission was detected in 57 out of 70 HzRGs; the non-detections are mainly at $z > 3$ and likely are a result of using a fixed integration time per object. This section examines the characteristics of the hot dust emission and what it can reveal about AGN activity. We selected a restframe wavelength of $5\,\mu$m in order to use a consistent luminosity throughout the redshift range in our sample. Contributions from stellar emission are negligible at this wavelength (see Appendix A).
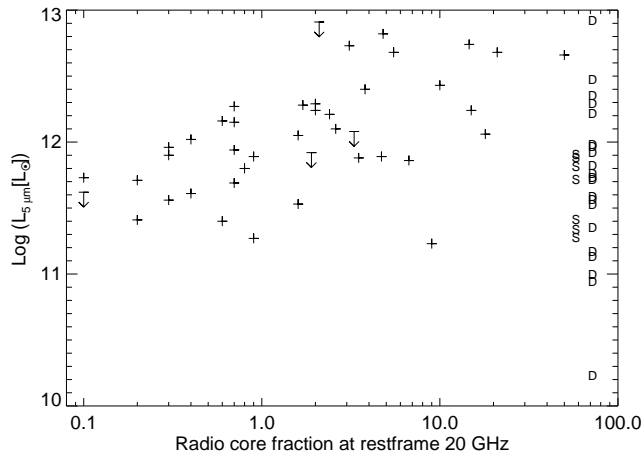
4.2.1. *Orientation effects*

Low-frequency radio emission is considered to be one of the most nearly isotropic components seen in distant AGNs. In contrast, mid-IR emission originates from the innermost regions of the torus and is expected to be much less isotropic due to obscuration effects. The mid-IR luminosity in type 2 AGNs does indeed appear to be fainter (= more obscured) than in type 1 AGNs from the same parent radio-selected samples, providing strong support for the orientation unification model (Shi et al. 2005; Haas et al. 2008; Leipski et al. 2010).

While our sample is also selected at low frequency, it contains only type 2 AGNs as determined from their restframe ultraviolet (observed visible) spectra. However, our mid-IR SEDs show a large variety, ranging

---

[15] Five of which are also in our SHzRG sample.

from clearly host-galaxy-dominated sources to SEDs that are almost indistinguishable from those of type 1 AGNs (Fig. 3). This suggests a gradual transition from highly obscured type 2 AGNs all the way to unobscured type 1 AGNs. To verify this hypothesis, we have checked whether radio morphological parameters can be used as independent indicators for orientation. Both radio size (e.g., Barthel 1989) and radio core dominance (e.g., Orr & Browne 1982) have been suggested as measures of orientation. The largest radio size, θ, and the hot-dust-dominated $L_{5\,\mu m}$ show a likely correlation ($P = 0.014$). This suggests that θ is probably an indicator of orientation but not a very reliable one. On the other hand, Figure 8 shows that the core fraction at restframe frequency 20 GHz, CF_{20}, is strongly correlated with $L_{5\,\mu m}$ ($P < 0.0001$). As we could determine core fractions of only 34 of our 70 sources, we caution that this analysis is not complete. Most of the 25 double-component sources have radio cores too faint to be detected in the current radio maps and are expected to have core fractions $CF_{20} << 1\%$. These 22 sources (marked by a 'D' on the righthand side of Fig 8) have a median $\langle \log(L_{5\,\mu m}/L_{\odot}) \rangle = 11.7$ and will fall close to the existing correlation. The remaining 8 single-component sources have a median $\langle \log(L_{5\,\mu m}/L_{\odot}) \rangle = 11.8$, but without higher spatial resolution observations we cannot estimate their CF_{20}. However, they represent only 11% of the sample and are unlikely to be able to remove the correlation completely. We now examine the physical origin of this correlation between the synchrotron-dominated radio emission and the hot dust dominated $\lambda_{\rm rest} = 5\,\mu m$ emission. (As argued in §3.2, a direct contribution from synchrotron emission at $\lambda_{\rm rest} = 5\,\mu m$ can be neglected.)

rect view of the inner parts of an obscuring torus perpendicular to the radio jet. This interpretation was recently confirmed by Leipski et al. (2010), who used *Spitzer*/IRS spectroscopy to show that the silicate absorption depth $\tau_{9.7\,\mu m}$ increases with decreasing radio core fraction (but see Landt et al. 2010 for a different view). Based on a sample of 31 3C radio galaxies, Ogle et al. (2006) claimed that radio morphology is *not* a reliable predictor of nuclear mid-IR luminosity. However, considering only their 13 "mid-IR luminous" radio galaxies, there does seem to be a correlation, consistent with our results which are based on a sample three times larger. If the radio jets in the more core-dominated and more luminous hot dust sources are indeed oriented closer to the line of sight, we would expect other anisotropic parameters to increase also. Examples include the equivalent widths of the [O II] $\lambda 3727$ Å and [O III] $\lambda 5007$ Å lines, both of which are known to correlate with radio core dominance in type 1 AGNs (Baker & Hunstead 1995). Deep restframe visible spectroscopy of our sample is currently underway and should be able to test this hypothesis (Nesvadba et al. 2011, in prep.).

We conclude that the radio core fraction is a powerful indicator of the expected mid-IR luminosity because it provides a measure of the obscuration. As a result, the spread in $L_{5\,\mu m}$ in our sample is in large part driven by obscuration/orientation effects with the most core-dominated sources being the least obscured ones.

Figure 9. Monochromatic luminosity at $5\,\mu m$ versus redshift. Horizontal bars indicate median luminosities in each of three redshift bins. Upper limits, indicated by arrows, cluster at $z > 3$ owing to the use of a fixed integration time for all sources.
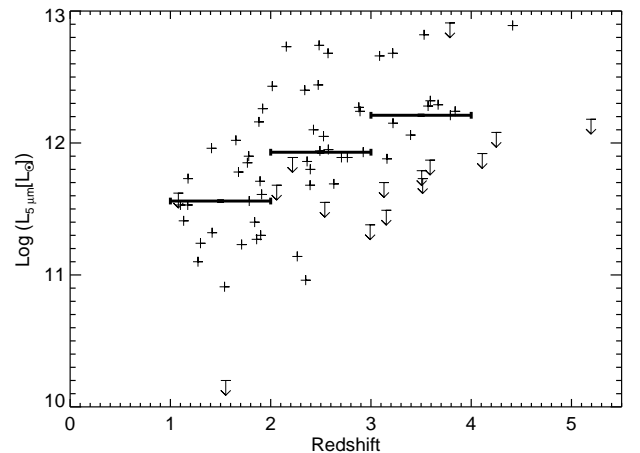

Figure 8. $5\,\mu m$ luminosity versus radio core fraction at restframe frequency 20 GHz. The $5\,\mu m$ luminosities of the double- and single-component radio sources that lack measurements of their core fractions are indicated on the right hand side of the plot by D and S respectively. The evident correlation indicates an orientation-dependence in our sample.

Higher core fraction sources are more strongly beamed, which can be understood if the radio jet is oriented closer along the line of sight of the observer (e.g., Orr & Browne 1982). These sources are therefore more similar to type 1 AGNs. The higher hot dust luminosity in them (Fig. 8) also indicates less obscuration, consistent with a more di-

4.2.2. *Evolutionary effects*

Figure 9 suggests a trend of rising restframe $5\,\mu m$ luminosity with redshift, which is confirmed by our generalized Spearman rank analysis ($P = 0.0021$). Before interpreting this correlation in terms of evolution of the dust content or emissivity, it is important to consider three selection effects. First, the $5\,\mu m$ luminosity is even more strongly correlated with radio power (see below), and there is a small remaining Malmquist bias in our radio-selected sample (see §2.1). This combined effect can amplify the redshift evolution of $L_{5\,\mu m}$, though it is unlikely

to imprint a correlation as strong as observed. Second, as shown in §4.3.1, orientation effects can strongly influence $L_{5\,\mu m}$. However, the core fractions are distributed quite evenly in redshift, suggesting that there is no redshift-dependent obscuration effect. Third, 9 out of 11 upper limits on $L_{5\,\mu m}$ are at $z > 3$ compared to 13 detections at $z > 3$. As shown by the survival analysis, the data still indicate a real correlation, though deeper mid-IR photometry at $z > 3$ will be needed to quantify the actual strength of the correlation. If confirmed, this would indicate that higher-redshift AGNs are more efficient in heating dust.

4.2.3. Correlation with radio power

Several authors have compared the hot dust emission from distant radio-loud AGNs at $8 < \lambda_{\rm rest} < 30\,\mu m$ with the $178\,{\rm MHz}$ radio luminosity (e.g., Shi et al. 2005; Ogle et al. 2006; Cleary et al. 2007; Haas et al. 2008). They found that type 1 AGNs show a clear positive correlation with a scatter of roughly an order of magnitude. Type 2 AGNs show more scatter and generally fainter hot dust emission because of obscuration, though the upper end of the type 2 range reaches the locus of the type 1 AGNs. Figure 10 plots $5\,\mu m$ luminosity against $500\,{\rm MHz}$ radio luminosity density for our sample and shows a strong correlation ($P < 0.0001$). The correlation is equally significant when using the $3\,{\rm GHz}$ luminosity instead. Obscuration will scatter sources downwards in Fig. 10, and it is remarkable that the observed correlation is so strong despite the orientation effects discussed in §4.3.1. We can get an idea of the intrinsic scatter by considering only the sources with $\log L_{5\,\mu m}/L_\odot > 12.5$, which are likely to experience only minimal extinction. These 8 sources cover a range of radio powers $28.3 < \log L_{500\,{\rm MHz}} < 29.3$. If all sources within this radio power range have the same intrinsic $\log L_{5\,\mu m}$, they exhibit up to 2 orders of magnitude of extinction. The fact that none of the 23 sources with $\log L_{500\,{\rm MHz}} < 28.3$ has $\log L_{5\mu m}/L_\odot > 12.5$ indicates that the ratio $L_{5\,\mu m}/L_{500\,{\rm MHz}}$ has an upper limit around a few hundred (see dotted lines in Fig. 10). However, it is impossible to determine the intrinsic spread in $L_{5\,\mu m}/L_{500\,{\rm MHz}}$ because of the range of extinction in $L_{5\,\mu m}$. Orientation effects will increase the spread in the $L_{5\,\mu m}$–$L_{500\,{\rm MHz}}$ plane, and the intrinsic correlation may be even stronger than observed.

The $L_{5\,\mu m}$–$L_{500\,{\rm MHz}}$ correlation implies that both are related to the energy output of the SMBH despite the vastly different spatial scales of the emission. The hot dust emission originates from the inner regions of the host galaxy near the SMBH on scales which may be as small as a few pc (e.g., Jaffe et al. 2004), while the radio luminosity is dominated by the extended radio lobes often extending beyond the host galaxy and reaching scales up to hundreds of kpc (Table 2). It is therefore remarkable that the scatter in the relation is limited to only two orders of magnitude. Naively, one might have expected a much larger spread, as it may be influenced by several effects such as (i) orientation effects as discussed above, (ii) different Eddington accretion rates onto the SMBH, (iii) time delays related to the very different size scales of the emitting regions, (iv) different dust distributions or compositions (e.g., in 6C 0032+412, see §4.1.2), and (v) environmental effects related to the medium in
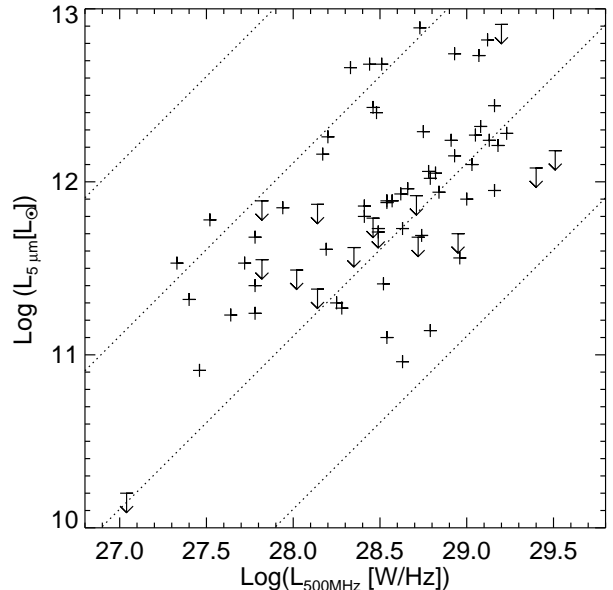
Figure 10. Restframe $5\,\mu m$ luminosity against monochromatic $500\,{\rm MHz}$ luminosity. Dotted lines indicate mid-IR to radio ratios of 1, 10, 100 and 1000 (bottom to top).

which the extended radio sources are expanding. The fact that the radio luminosity is more strongly correlated with hot dust emission than with the stellar mass of the host galaxy (§4.2.1) suggests that variations in the Eddington ratio of the AGN may be the dominant factor in driving both the radio power and hot dust emission. Hickox et al. (2009) and Griffith & Stern (2010) also suggest that radio-loud AGNs show a larger range in Eddington luminosity than X-ray and mid-IR selected AGNs.

4.2.4. Absence of a correlation with stellar mass

Does hot dust emission depend on the mass of the host galaxy? Figure 11 plots the hot dust dominated $5\,\mu m$ luminosity against stellar mass, showing that the two are uncorrelated ($P = 0.73$). The upper limits in the top right corner illustrate the success of our color-color selection criterion to identify hot dust dominated SEDs (§3.3, Fig. 4). The absence of a correlation also suggests that AGN luminosity is independent of stellar mass, though we warn that orientation effects (§4.2.1) make $L_{5\,\mu m}$ not a reliable measure of AGN luminosity.

4.3. Notes on individual sources

Radio galaxies are often complex systems consisting of several components. Therefore, our *Spitzer* photometry is occasionally affected by companion and/or foreground objects. We have visually inspected the six-band *Spitzer* images for our entire sample, using multi-wavelength data in the literature to determine the correct astrometric identifications as listed in Table 1. In most cases, we found an unambiguous radio source counterpart. The next two subsections describe all special cases, first sources with multiple AGNs (§4.3.1) followed by detailed discussions of a few additional interesting sources (§4.3.2).

4.3.1. Binary AGNs
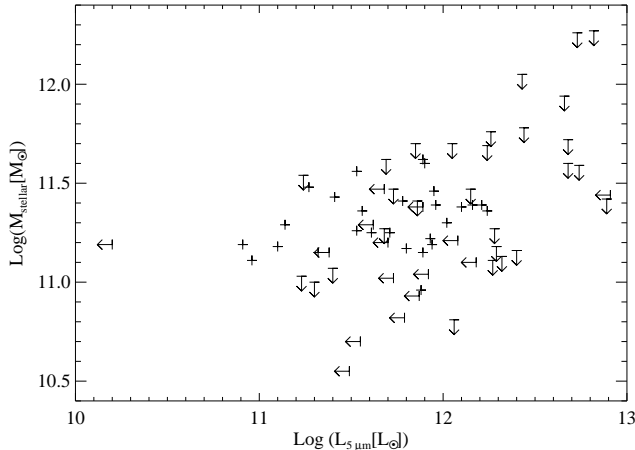
Figure 11. Stellar mass versus $5\,\mu$m luminosity. The lack of correlation implies that our criteria to isolate hot-dust dominated SEDs are successful and that stellar mass is uncorrelated with $5\,\mu$m luminosity.

As shown in §4, HzRGs are massive galaxies hosting a SMBH. If such massive galaxies are formed in a series of merger events as predicted by the standard Λ Cold Dark Matter paradigm, we expect that merging massive galaxies will coincide with merging central SMBHs (e.g., Comerford et al. 2009). Observationally, this may manifest itself as a second AGN near the HzRG, or — at later stages in the merger event — by perturbed morphologies as observed in low redshift radio galaxies (e.g., Ramos Almeida et al. 2010). The low spatial resolution of *Spitzer*, particularly at the longest wavelengths, limits such studies to companion AGNs at many-kpc distances rather than the sub-kpc separations in later stages of merging. The mid-IR images show evidence for a second AGN in four HzRGs in our sample (Fig. 12; discussed in RA order):

4C 60.07 (z = 3.788): Ivison et al. (2008) showed that this system consists of two AGNs separated by $4''$ (30 kpc). The radio galaxy (A), as identified by the radio core, remains undetected in the hot dust emission beyond $4.5\,\mu$m, while the companion object B, which currently lacks a spectroscopic redshift, has very red hot dust emission characteristic of an obscured AGN. An initial claim of a CO(1-0) redshift for this second AGN (Greve et al. 2004) could not be confirmed in the re-analysis of those data (Ivison et al. 2008), but the (sub)mm dust continuum morphology looks consistent with both targets being at the same redshift.

3C 356 (z = 1.079): There are two potential identifications for the location of the radio-loud AGN. Based on the detection of scattered broad line regions with a polarization angle perpendicular to the "dumbell" structure of the galaxy, Simpson & Rawlings (2002) argued that the northwestern object a is the most likely location, but object b, offset by $4''5$ (36 kpc), may also contain an AGN. Both targets were spectroscopically confirmed to be at $z = 1.079$. Cimatti et al. (1997) showed that object a has a high restframe UV polarization, clearly indicating the presence of a hidden AGN. We detected both objects in all four IRAC bands, though only object a has strong mid-IR dust emission seen with IRS and MIPS. This provides further support for the conclusion that object a is

the location of the radio galaxy host, while object b is a companion object. Tables 3 and 5 list the photometry for both objects.

7C 1756+6520 (z = 1.416,): Galametz et al. (2009) found three objects within $6''$ (48 kpc) of the radio galaxy, two of which were spectroscopically confirmed by Galametz et al. (2010) to be at the same redshift as the radio galaxy. One of them is a mid-IR selected AGN. Both this AGN and a passively evolving BzK-selected (pBzK) galaxy were individually detected with IRAC but only marginally resolved with IRS and MIPS. Tables 3 and 5 provide photometry of both objects; as the HzRG and AGN are not fully spatially resolved in the IRS $16\,\mu$m and MIPS $24\,\mu$m images, we estimated the relative fluxes between the HzRG and AGN by summing the pixel values in a fixed circular 6 pixel radius aperture using the positions from the IRAC $3.6\,\mu$m image (Fig. 12) as centroids. The derived ratios of 50%/50% at $16\,\mu$m and and 20%/80% at $24\,\mu$m should be considered approximative. This paper uses the revised redshift of the HzRG from Galametz et al. (2010).

MRC 2048−272 (z = 2.060): No radio or X-ray core was detected in this radio galaxy (Carilli et al. 1997; Overzier et al. 2005). Pentericci et al. (2001) detected two sources, separated by $2''5$ (21 kpc), in NICMOS H-band imaging and considered the easternmost one as the most likely AGN host. This is consistent with the Lyα halo, which extends for $\sim 5''$ along the radio axis (Venemans et al. 2007). We detected both components in the IRAC 3.6 and $4.5\,\mu$m images. However, at longer wavelengths only the western source is detected, suggesting it also contains an AGN. This configuration is reminiscent of 4C 60.07.

4.3.2. *Other Sources*

6C 0032+412 (z = 3.670): This HzRG is the only one where our standard 3-component dust model (using $T = 60$, 250, and 500–1500 K, see §3.2) could not fit the SED. First, we had to increase the temperature of the $T = 250$ component to $T = 650$ K. In addition, this is the only source where we required $T = 1500$ K for the hottest dust component compared to a median $\langle T \rangle = 800$ K . A near-IR bump caused by a $T \sim 1500$ K dust component has been seen in several quasars (e.g., Gallagher et al. 2007; Mor et al. 2009; Leipski et al. 2010) and is generally associated with graphite dust near the sublimation temperature (e.g., Barvainis 1987). The very high temperature necessarily locates the dust very close to the AGN. Leipski et al. (2010) argued that this very hot dust emission is either more highly extincted or completely absent in radio galaxies. While this object is the only example in our sample, it does represent the first counterexample to the radio galaxy trend. 6C 0032+412 is a bona-fide type 2 AGN as derived from its narrow-line UV and visible spectroscopy (Jarvis et al. 2001). The modest 2% radio core fraction (Table 2) also does not indicate a line of sight close to that of quasars (see §4.3.1). A possible explanation would be that 6C 0032+412 presents a rare unobscured line of sight through the entire dusty torus all the way to the central regions near the AGN.

MRC 0037−258 (z = 1.10): The new radio imaging clearly detected the radio core at 4.86 and 8.46 GHz.

MRC 0114−211 (z = 1.41): We identify the faint central component, which is spatially resolved only in the
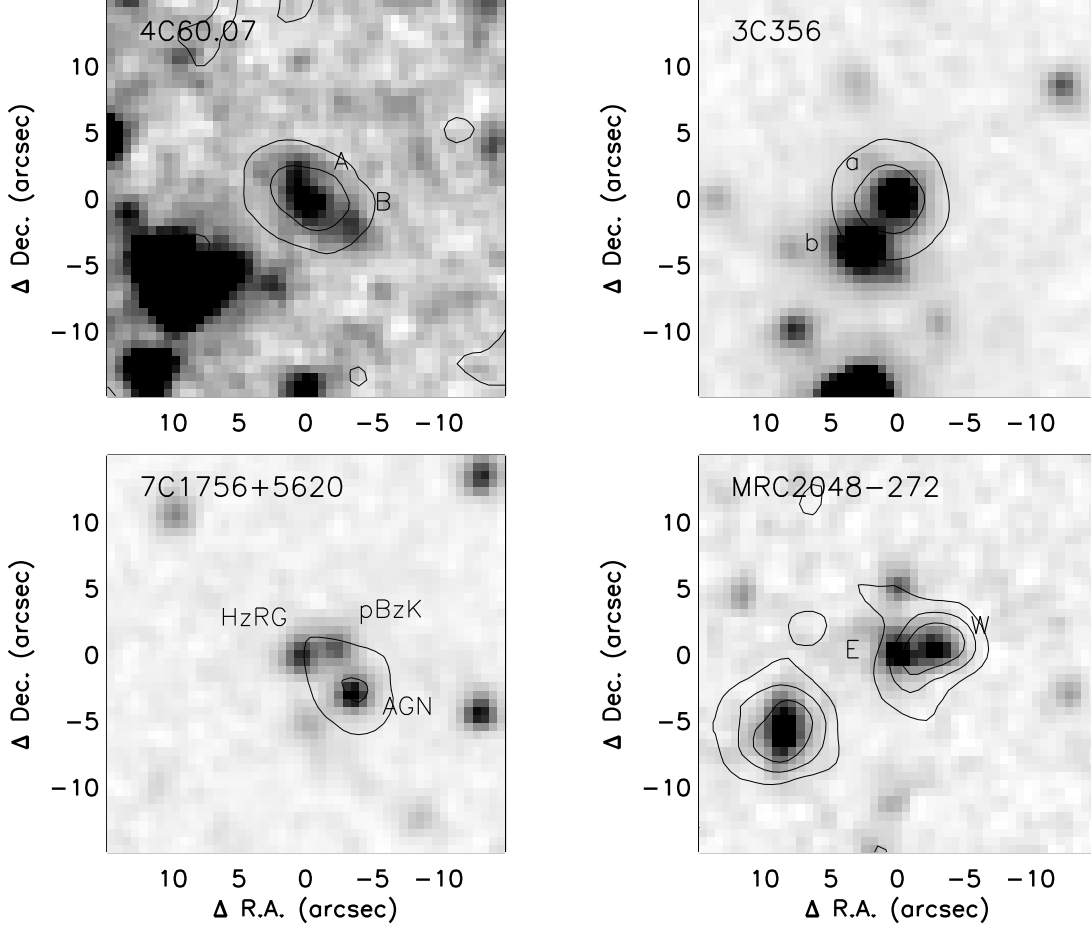
Figure 12. *Spitzer*/IRAC 3.6 μm images of the four binary AGNs in our sample. Contours show the MIPS 24 μm images. Photometry for the HzRG and companions are listed in Tables 3 and 5, respectively.

8.46 GHz map, as the core.

6C* 0132+330 (z = 1.71): We identify the central component seen at both frequencies as the radio core.

6C 0140+326 (z = 4.41): Rawlings et al. (1996) argued that this radio galaxy is gravitationally lensed by a foreground (z = 0.927) galaxy 1″6 to the southeast. This foreground L_* galaxy has an ellipsoidal shape in both the Keck/NIRC K-band image (van Breugel et al. 1998) and the *HST*/NICMOS F160W image (Lacy 1999). Our *Spitzer* photometry at 3.6 and 4.5 μm is dominated by strong a strong foreground star, while the 16 and 24 μm photometry are dominated by mid-IR emission from the lensing galaxy. The radio galaxy itself appears undetected in all but the 5.8 or 8 μm emission, where it is only marginally detected and contaminated by the foreground galaxy. We therefore provide only relatively shallow upper limits based on the detection of the foreground galaxy.

MRC 0251−273 (z = 3.16): Our radio map (Appendix B) shows five bright components at 8.46 GHz as well as diffuse emission to the north-northwest (mainly at 4.85 GHz). The lower-resolution radio map of Kapahi et al. (1998) confirms that this diffuse emission is real. Within the radio structure, there is only a single IRAC identification, coinciding within 0″3 with the northernmost of the bright components in the 8.46 GHz

map. We therefore identify this component as the radio core. This radio morphology resembles that of B2 0902+34 (Carilli 1995). The radio jet is probably aligned relatively closely to the line of sight, with the complex south-southeastern radio structure being the approaching radio jet.

MRC 0324−228 (z = 1.894): The NICMOS image of this radio galaxy (Pentericci et al. 2001) reveals two potential host galaxies separated by 1″5 (12 kpc). Our *Spitzer* imaging does not resolve them as individual sources, though it does show an extended structure along the same north–south orientation. Our new radio data tentatively detected a faint radio core at 4.86 GHz, coinciding with the southernmost of these two identifications, which we have adopted as the host galaxy. There are also two nearby objects that may contaminate the MIPS photometry.

MRC 0350−279 (z = 1.90): No radio core is detected in our new radio maps.

5C 7.269 (z = 2.218): No radio core is detected in our new radio maps.

6C 0820+3642 (z = 1.860): The new radio imaging detects a faint radio core, which is most obvious in the 8.46 GHz map.

6C 0901+3551 (z = 1.91): No radio core is detected in our new radio maps.

USS 1243+036 (z = 3.570): Our *Spitzer* photometry is not sufficiently sensitive to exclude a possible contribution from hot dust at rest-frame $1.6\,\mu$m. The derived stellar masses are therefore formally considered as upper limits, although the 3.5 and $4.5\,\mu$m photometry suggests they are most likely uncontaminated by hot dust.

USS 1707+105 (z = 2.349): The new radio imaging detects a faint radio core, which is most obvious in the 4.86 GHz map.

LBDS 53W002 (z = 2.293): The IRS and MIPS photometry are possibly contaminated by a galaxy $\sim4''$ to the northwest (Keel et al. 2002). This galaxy is most likely at a different redshift than the AGN host as it does not appear in the [O III] and Hα narrow-band imaging of Keel et al. (2002).

7C 1751+6809 (z = 1.54): No radio core is detected in our new radio maps.

7C 1805+6332 (z = 1.84): The new radio imaging detects a faint radio core, which is only seen in the 8.46 GHz map.

TXS J1908+7220 (z = 3.530): Using integral field spectroscopy, Smith et al. (2010) argued that this broad line radio galaxy is a system of two vigorously star-forming galaxies superimposed along the line of sight and separated by $\sim$1300 km s^{-1} in velocity. The detailed SED decomposition of Smith et al. (2010) also showed that the near-IR emission of this HzRG is dominated by transmitted quasar continuum. While the hot dust continuum does not contribute substantially at $\lambda_{\rm rest} = 1.6\,\mu$m, this transmitted quasar continuum prevents us from measuring the old stellar population, and we provide only an upper limit to the stellar mass.

TN J2007-1316 (z = 3.84): We identify the second component from the north as the radio core. This component is spatially resolved only in the 8.46 GHz map.

MG 2144+1928 (z = 3.592): Our *Spitzer* photometry is not sufficiently sensitive to exclude a possible contribution from hot dust at rest-frame $1.6\,\mu$m. The derived stellar masses are therefore formally considered as upper limits, although the 3.5 and $4.5\,\mu$m photometry suggests they are most likely uncontaminated by hot dust.

5. SUMMARY AND CONCLUDING REMARKS

The main results from our full six-band *Spitzer* imaging survey of 70 radio galaxies at $1 < z < 5.2$ can be summarized as follows:

1. Using a newly designed criterion to isolate sources dominated by hot dust emission at $\lambda_{\rm rest}$=1.6$\,\mu$m, we unambiguously detect a stellar population in 46 radio galaxies and hot dust emission in 59.

2. Four of the 70 HzRGs show a second AGN within $6''$, as revealed by their mid-IR colors. This may be an indication of an ongoing or imminent major merger event.

3. The stellar masses have a remarkably low scatter around $\sim 2 \times 10^{11}\,{\rm M}_\odot$. There is tentative evidence for a small drop in stellar mass at $z > 3$. If confirmed by more detailed spectral decompositions, this result suggests that radio galaxies have built the bulk of their stellar populations by $z \sim 3$. This is consistent with the observed increase in their submillimeter luminosities, suggesting higher star formation rates, at $z > 3$.

4. The radio core fraction is strongly correlated with restframe $5\,\mu$m luminosity. The most core-dominated radio galaxies are also the most luminous (i.e., least obscured) hot dust emitters. This suggests a gradual increase of the hot dust obscuration from type 2 to type 1 AGNs, consistent with the orientation paradigm of AGN unification. It also complicates the use of $\lambda_{\rm rest} = 5\,\mu$m luminosity as an indicator of AGN power.

5. The 500 MHz radio luminosity is only marginally correlated with stellar mass but strongly correlated with the hot dust luminosity at $\lambda_{\rm rest} = 5\,\mu$m. Variations in the Eddington ratio of the SMBH could explain these trends.

Our *Spitzer* sample provides an unique database to study the massive host galaxies of powerful radio galaxies, their AGN-heated dust emission, as well as their environments. In future papers we plan to study the stellar populations in greater detail by combining the *Spitzer* data with visible and near-infrared data to better constrain the HzRG star formation histories and thus derive more accurate stellar masses and ages. We also plan to observe the cold dust component with the Atacama Large Millimeter and submillimeter Array (ALMA) and the peak of the dust emission with *Herschel Space Observatory*. This full SED will allow to separate the hot AGN from the cool, starburst-heated dust emission, providing more accurate measures of the instantaneous star formation rates. This combined dataset will provide a unique view of the star formation history in these very massive galaxies at every epoch.
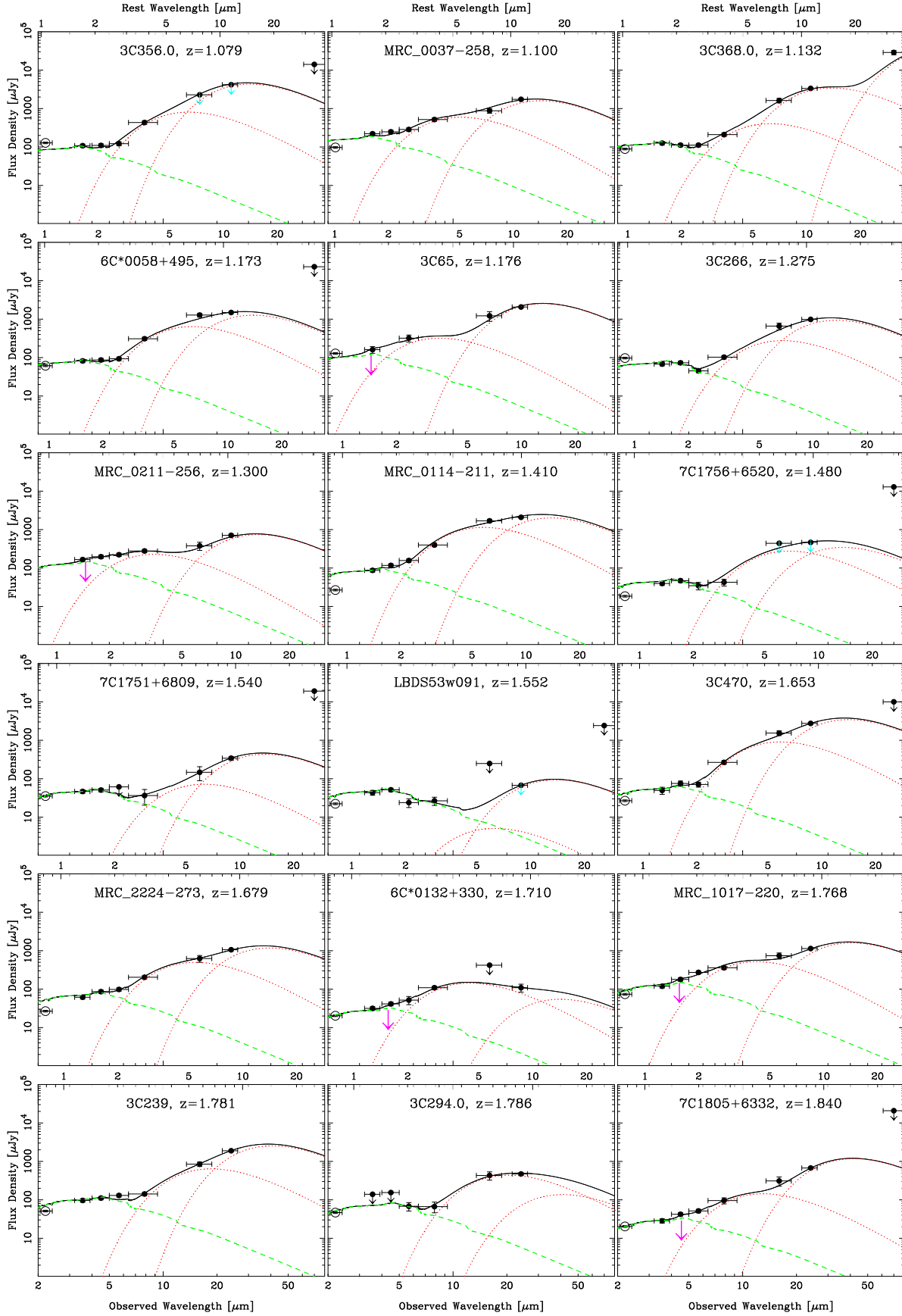
APPENDIX

SED FITS TO RADIO GALAXIES AND NOTES ON INDIVIDUAL SOURCES

Figure 13 presents the *Spitzer* SEDs for our complete HzRG sample, including model fits to the mid-IR photometry, ordered by redshift.

Figure 13. Radio galaxy SEDs and model fits. Lower abscissas are marked with observed wavelengths, and the scales are the same for all objects. Upper abscissas are marked with restframe wavelengths, which depend on wavelength for each object. Filled circles with error bars denote data points used in the fit; open circles denote data points that could be contaminated by emission lines and are therefore not used in the fits. Model components are a stellar population (green dashed lines) and two or three pure blackbodies (red dotted lines) representing dust emission. The sum of the model components is shown by solid black line. The name and redshift of each target is marked at the top of the panel. A downward arrow at $\lambda_{rest}=1.6$ or $5\,\mu m$ indicates an upper limit on the stellar or hot dust emission, respectively.
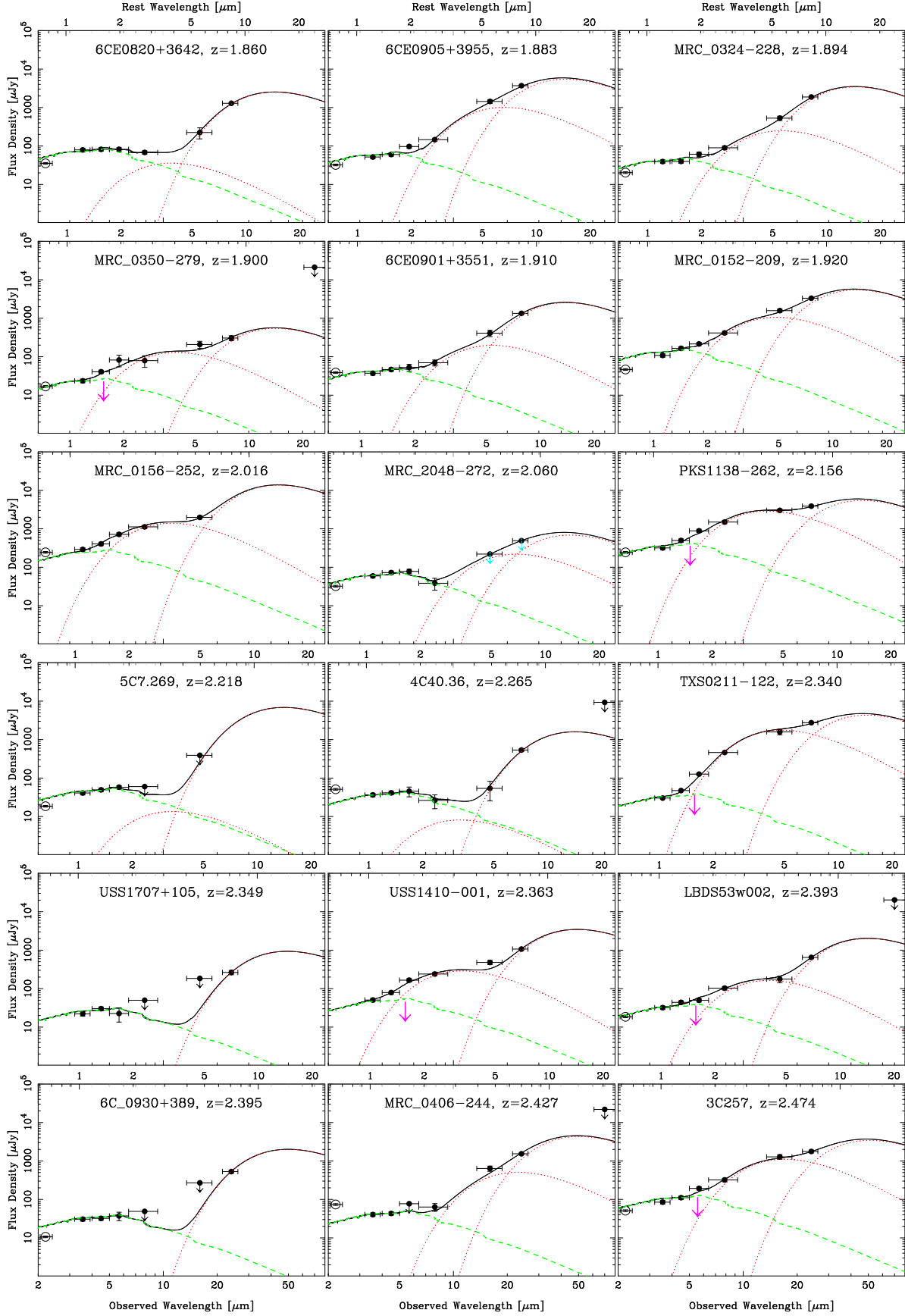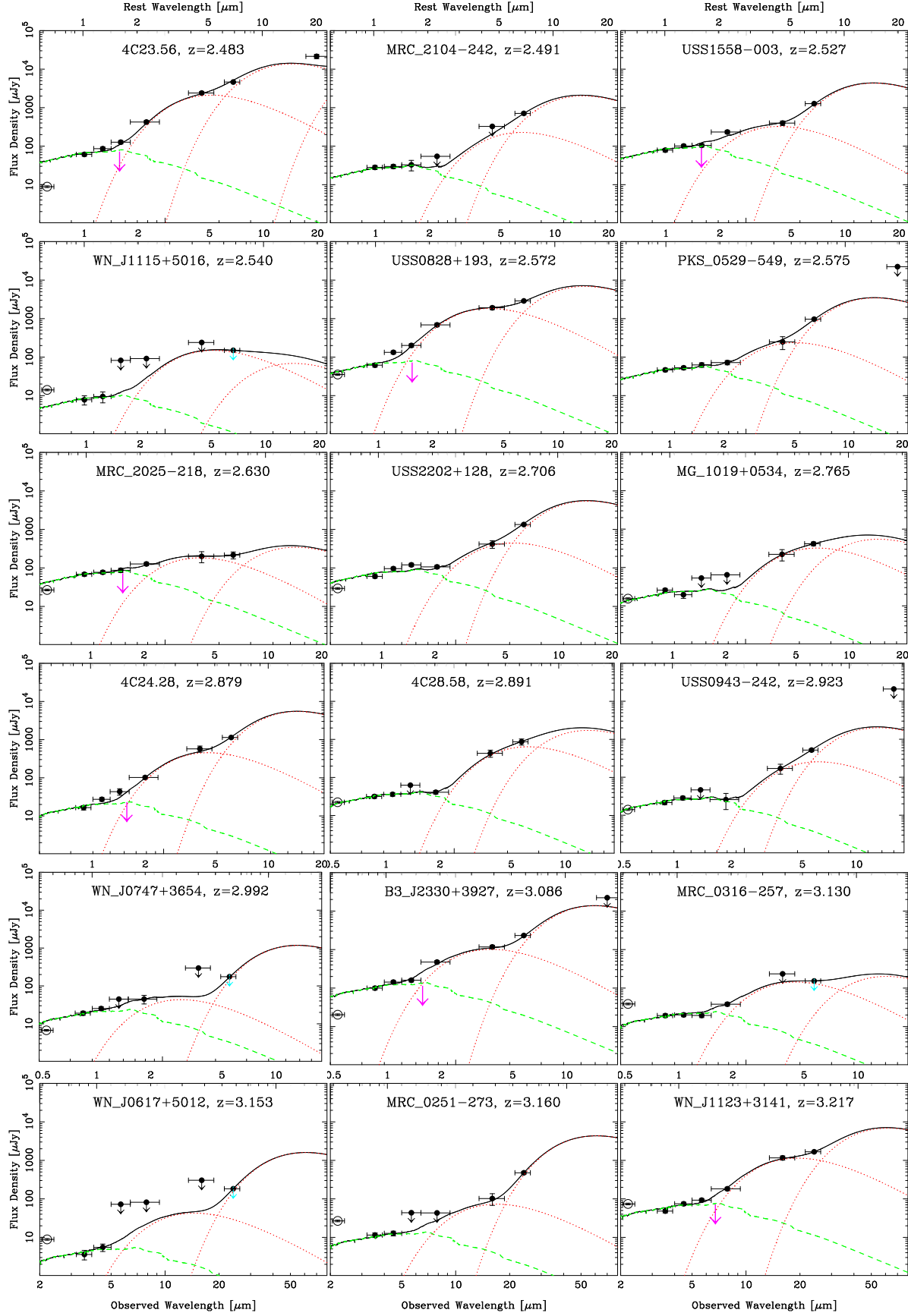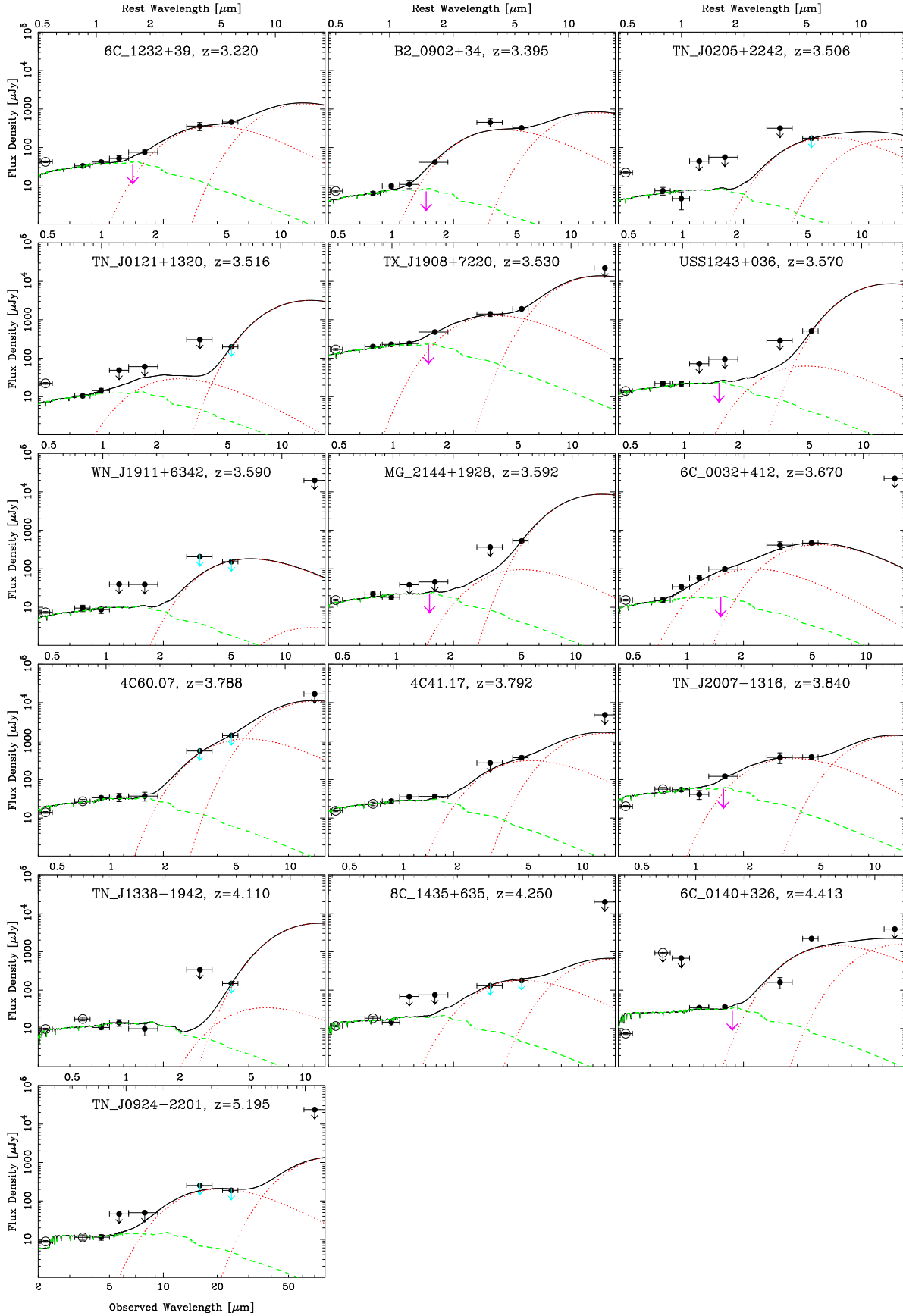
NEW RADIO MAPS OF SOURCES IN OUR SAMPLE

Figure 14 presents the new VLA A-array radio maps.
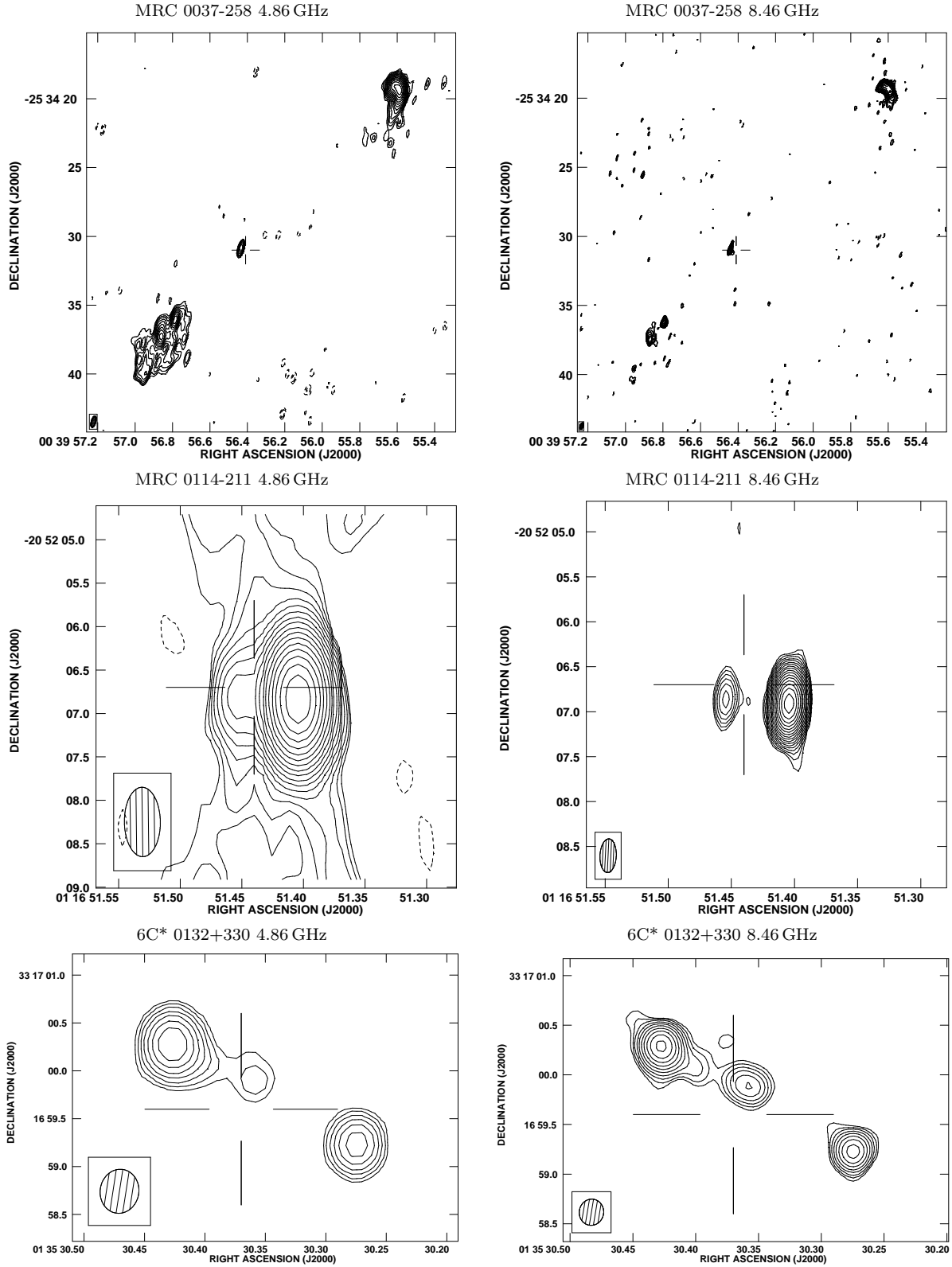
Figure 14. VLA 4.86 and 8.46 GHz images of 14 HzRGs in our sample. The contour scheme is a geometric progression of $\sqrt{2}$, with the first contour starting at 3σ. Open crosses mark the near-IR identification position listed in Table 1.

MRC 0251-273 4.86 GHz
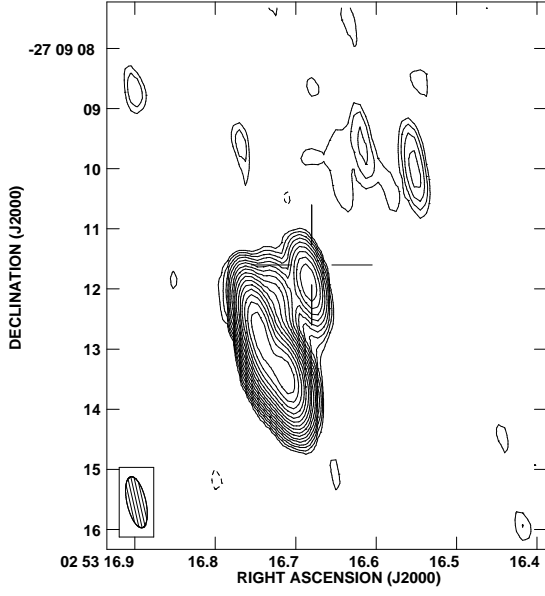
MRC 0251-273 8.46 GHz
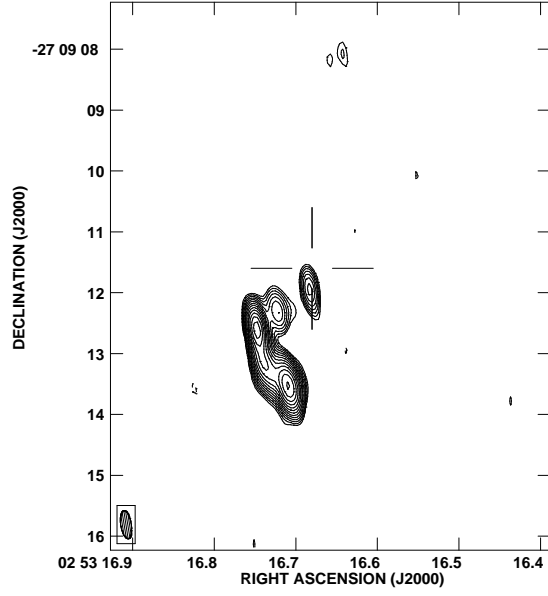
MRC 0324-228 4.86 GHz
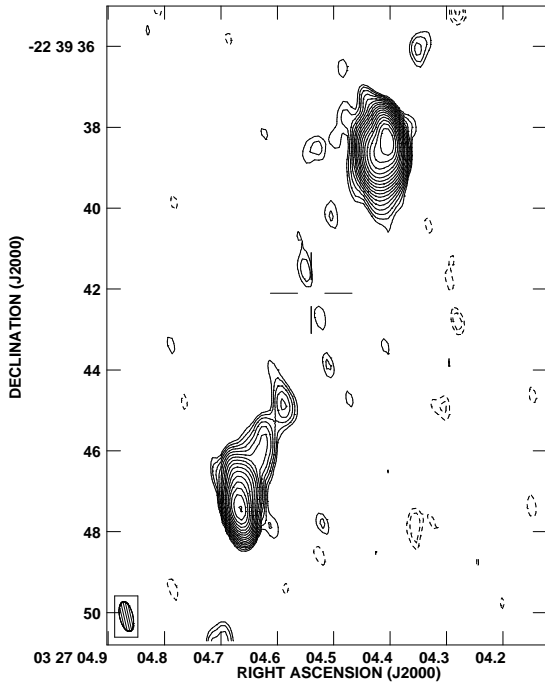
MRC 0324-228 8.46 GHz
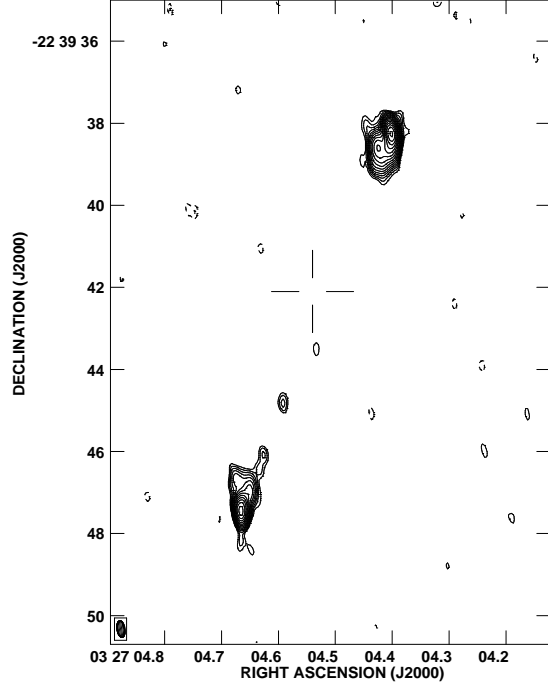
MRC 0350-279 4.86 GHz

MRC 0350-279 8.46 GHz

5C 7.269 4.86 GHz

5C 7.269 8.46 GHz

6C 0820+3642 4.86 GHz

6C 0820+3642 8.46 GHz

6C 0901+3551 4.86 GHz
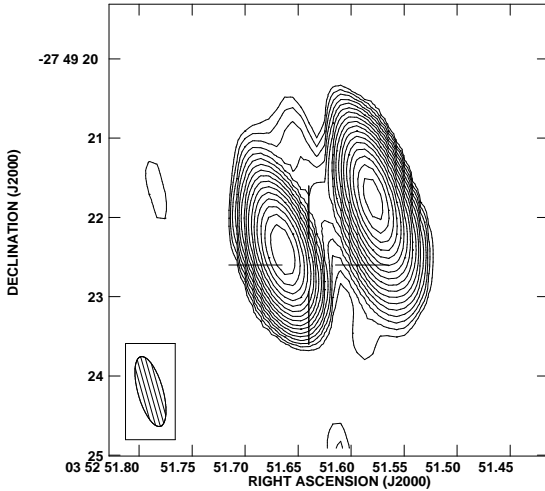
6C 0901+3551 8.46 GHz
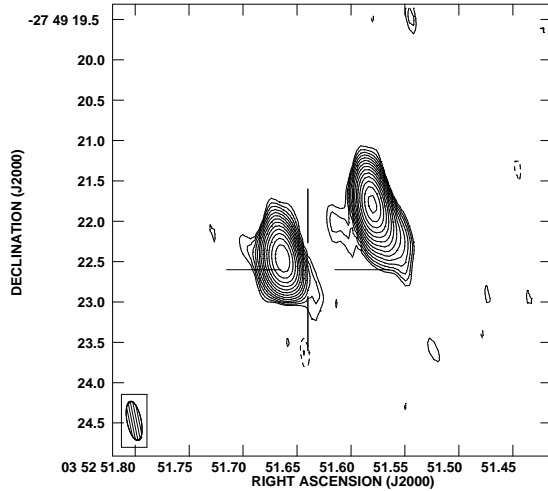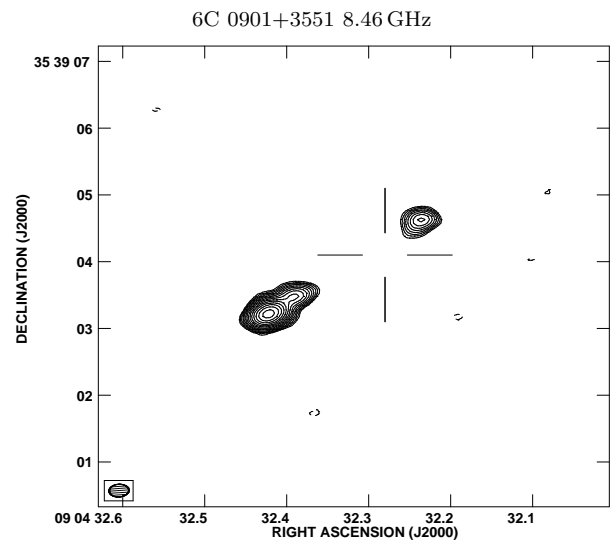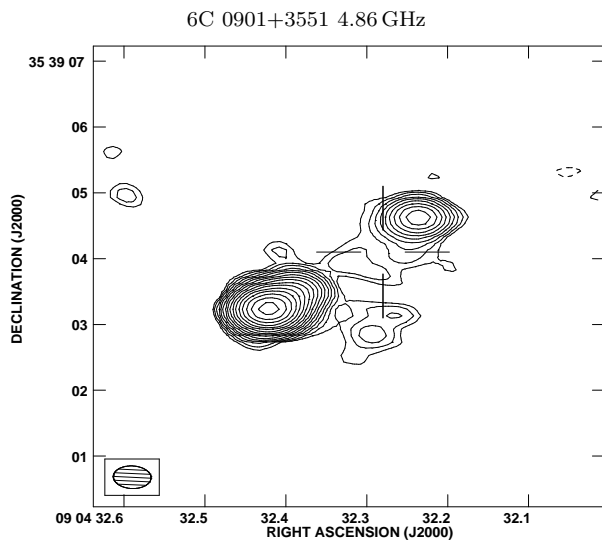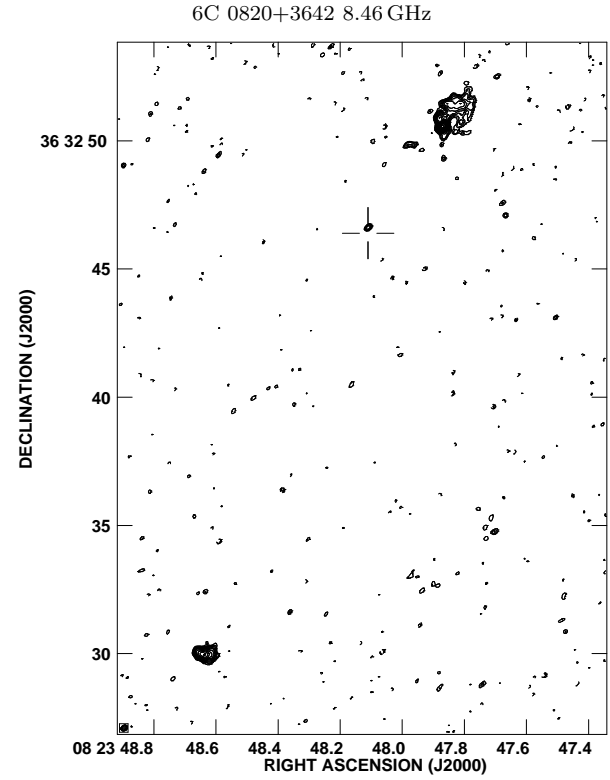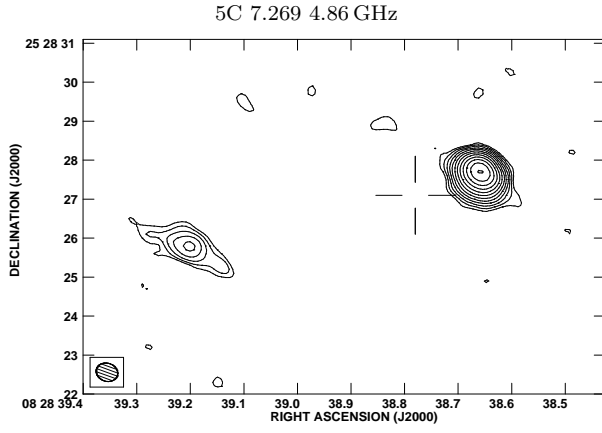
USS 1707+105 4.86 GHz

USS 1707+105 8.46 GHz

7C 1751+6809 4.86 GHz

7C 1751+6809 8.46 GHz

7C 1756+6520 4.86 GHz

7C 1756+6520 8.46 GHz

7C 1805+6332 4.86 GHz

7C 1805+6332 8.46 GHz

TN J2007-1316 4.86 GHz
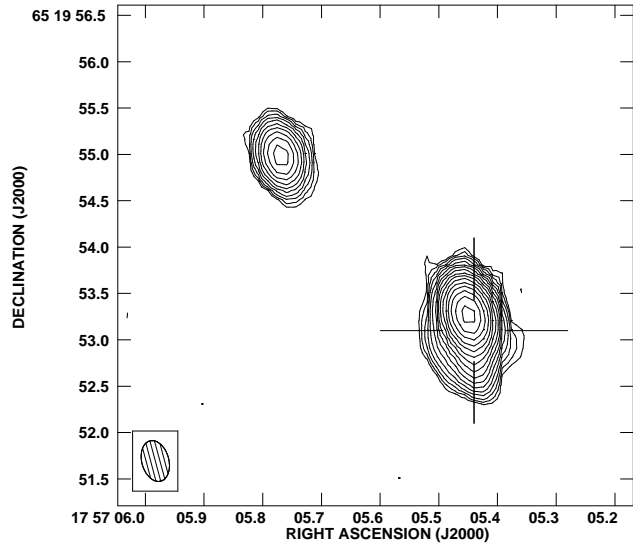
TN J2007-1316 8.46 GHz
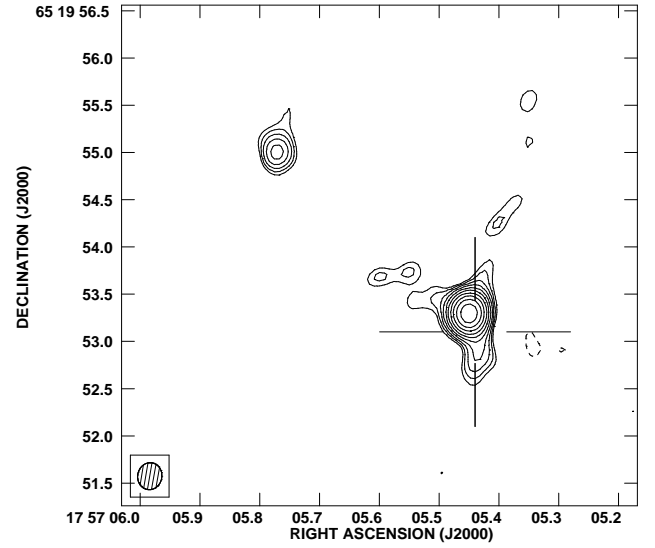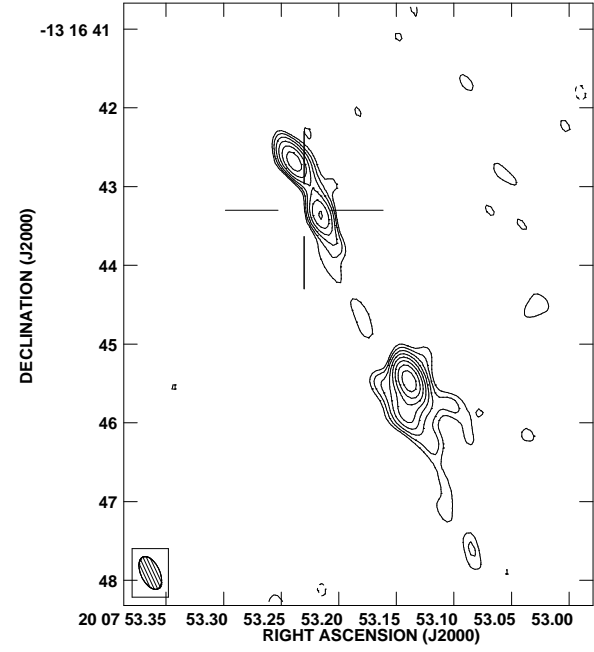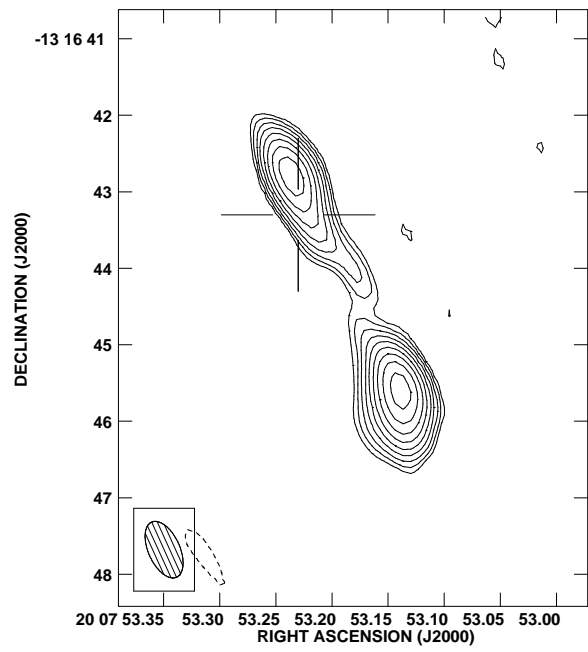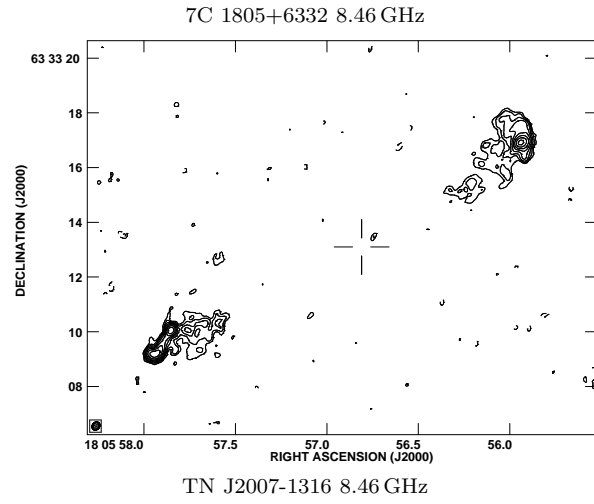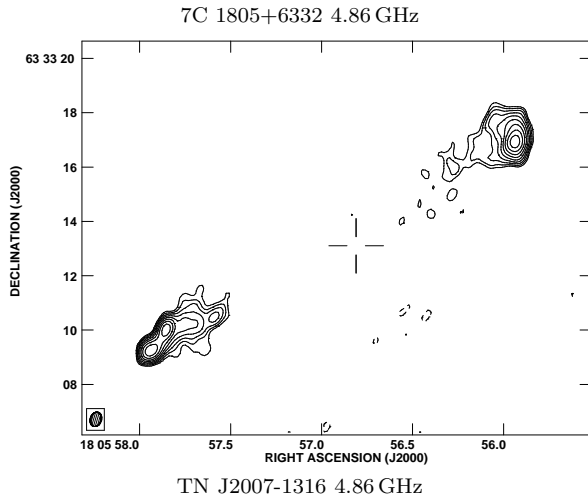
REFERENCES

Andreani, P., Fosbury, R. A. E., van Bemmel, I., & Freudling, W. 2002, A&A, 381, 389

Archibald, E. N., Dunlop, J. S., Hughes, D. H., Rawlings, S., Eales, S. A., & Ivison, R. J. 2001, MNRAS, 323, 417

Assef, R. J., et al. 2010, arXiv:1001.4529

Athreya, R. M., Kapahi, V. K., McCarthy, P. J., & van Breugel, W. 1997, MNRAS, 289, 525

Baker, J. C., & Hunstead, R. W. 1995, ApJ, 452, L95

Barthel, P. D. 1989, ApJ, 336, 606

Barvainis, R. 1987, ApJ, 320, 537

Best, P. N., Longair, M. S., & Röttgering, J. H. A. 1997, MNRAS, 292, 758

Best, P. N., Longair, M. S., & Röttgering, H. J. A. 1998, MNRAS, 295, 549

Bîrzan, L., McNamara, B. R., Nulsen, P. E. J., Carilli, C. L., & Wise, M. W. 2008, ApJ, 686, 859

Bîrzan, L., McNamara, B. R., Nulsen, P. E. J., Carilli, C. L., & Wise, M. W. 2010, ApJ, 709, 546

Blundell, K. M., Rawlings, S., Eales, S. A., Taylor, G. B., & Bradley, A. D. 1998, MNRAS, 295, 265

Broderick, J. W., De Breuck, C., Hunstead, R. W., & Seymour, N. 2007, MNRAS, 375, 1059

Brookes, M. H., Best, P. N., Rengelink, R., & Röttgering, H. J. A. 2006, MNRAS, 366, 1265

Bryant, J. J., Johnston, H. M., Broderick, J. W., Hunstead, R. W., De Breuck, C., & Gaensler, B. M. 2009, MNRAS, 395, 1099

Cai, Z., et al. 2002, A&A, 381, 401

Carilli, C. L., Owen, F. N., & Harris, D. E. 1994, AJ, 107, 480

Carilli, C. L. 1995, A&A, 298, 77

Carilli, C. L., Röttgering, H. J. A., van Ojik, R., Miley, G. K., & van Breugel, W. J. M. 1997, ApJS, 109, 1

Cattaneo, A., & Best, P. N. 2009, MNRAS, 395, 518

Cavagnolo, K. W., McNamara, B. R., Nulsen, P. E. J., Carilli, C. L., Jones, C., & Birzan, L. 2010, arXiv:1006.5699

Chambers, K. C., Miley, G. K., van Breugel, W. J. M., Bremer, M. A. R., Huang, J.-S., & Trentham, N. A. 1996, ApJS, 106, 247

Cimatti, A., Dey, A., van Breugel, W., Hurt, T., & Antonucci, R. 1997, ApJ, 476, 677

Cleary, K., Lawrence, C. R., Marshall, J. A., Hao, L., & Meier, D. 2007, ApJ, 660, 117

Cohen, A. S., Lane, W. M., Cotton, W. D., Kassim, N. E., Lazio, T. J. W., Perley, R. A., Condon, J. J., & Erickson, W. C. 2007, AJ, 134, 1245

Comerford, J. M., Griffith, R. L., Gerke, B. F., Cooper, M. C., Newman, J. A., Davis, M., & Stern, D. 2009, ApJ, 702, L82

Condon, J. J., Cotton, W. D., Greisen, E. W., Yin, Q. F., Perley, R. A., Taylor, G. B., & Broderick, J. J. 1998, AJ, 115, 1693

Corbin, M. R., Charlot, S., De Young, D. S., Owen, F., & Dunlop, J. S. 1998, ApJ, 496, 803

De Breuck, C., van Breugel, W., Röttgering, H. J. A., & Miley, G. 2000, A&AS, 143, 303
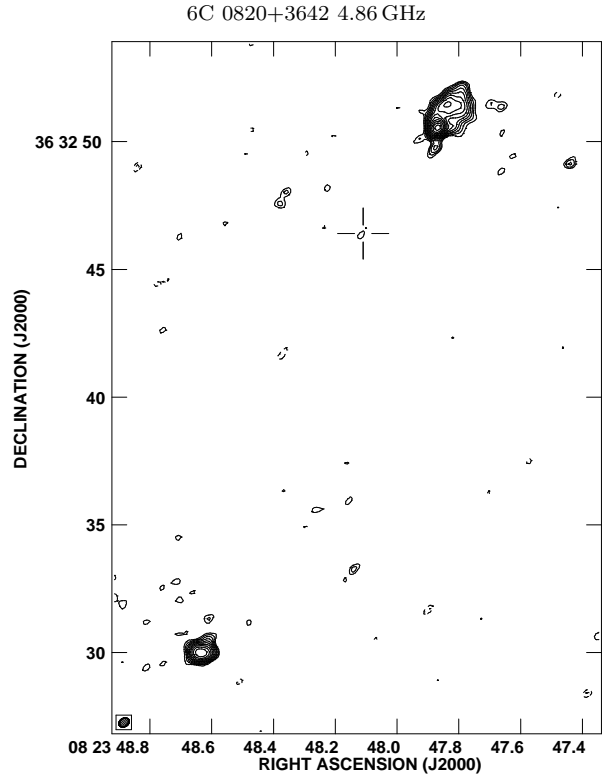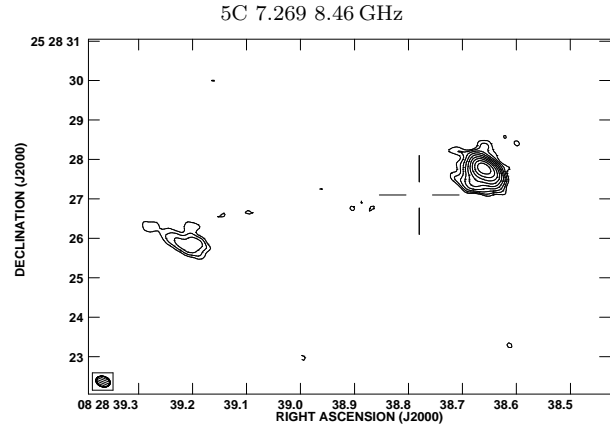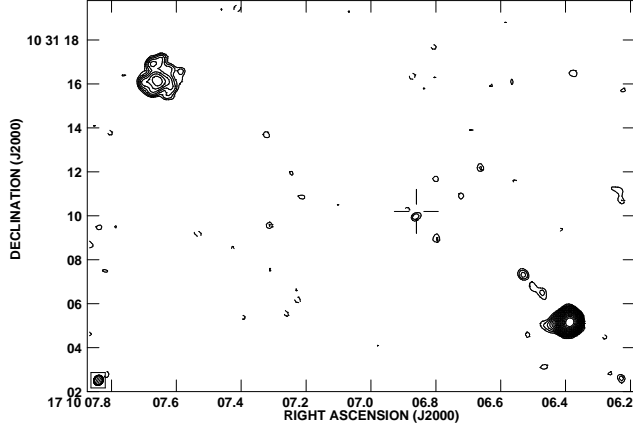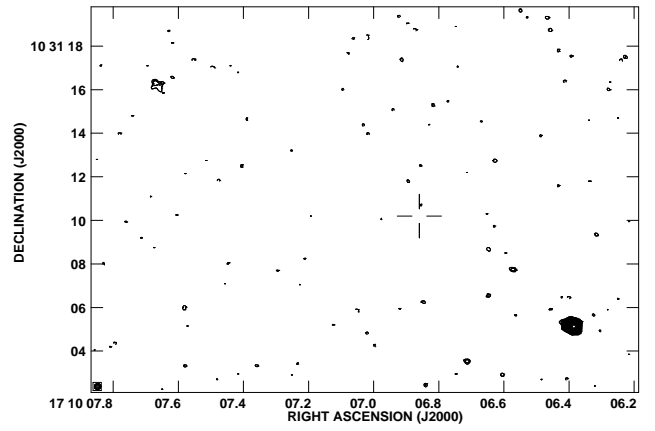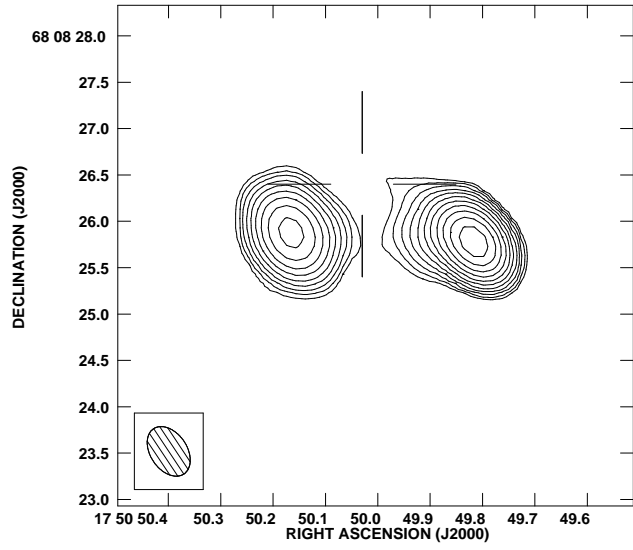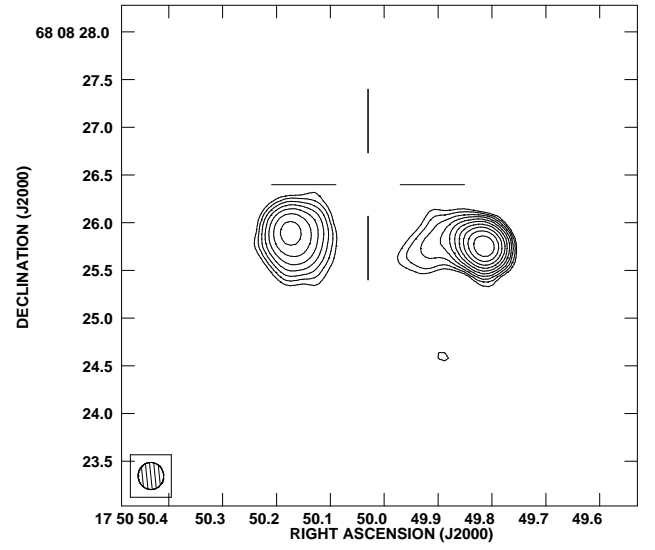
De Breuck, C., van Breugel, W., Stanford, S. A., Röttgering, H., Miley, G., & Stern, D. 2002, AJ, 123, 637

Devriendt, J. E. G., Guiderdoni, B., & Sadat, R. 1999, A&A, 350, 381

Dey, A., et al. 2008, ApJ, 677, 943

Doherty, M., et al. 2010, A&A, 509, A83

Douglas, J. N., Bash, F. N., Bozyan, F. A., Torrence, G. W., & Wolfe, C. 1996, AJ, 111, 1945

Eales, S., Rawlings, S., Law-Green, D., Cotter, G., & Lacy, M. 1997, MNRAS, 291, 593

Elitzur, M., & Shlosman, I. 2006, ApJ, 648, L101

Elvis, M., et al. 1994, ApJS, 95, 1

Fazio, G. G. et al. 2004, ApJS, 154, 10

Fioc, M., & Rocca-Volmerange, B. 1997, A&A, 326, 950

Fomalont, E. B., Kellermann, K. I., Partridge, R. B., Windhorst, R. A., & Richards, E. A. 2002, AJ, 123, 2402

Frater, R. H., Brooks, J. W., & Whiteoak, J. B. 1992, JEEE, Australia, 12, 2, p. 103

Fritz, J., Franceschini, A., & Hatziminaoglou, E. 2006, MNRAS, 366, 767

Galametz, A., et al. 2009, A&A, 507, 131

Galametz, A., Stern, D., Stanford, S. A., De Breuck, C., Vernet, J., Griffith, R. & Harrisson, F. 2010, A&A, 516, 101

Gallagher, S. C., Richards, G. T., Lacy, M., Hines, D. C., Elitzur, M., & Storrie-Lombardi, L. J. 2007, ApJ, 661, 30

Granato, G. L., Danese, L., & Franceschini, A. 1997, ApJ, 486, 147

Greve, T. R., Ivison, R. J., & Papadopoulos, P. P. 2004, A&A, 419, 99

Greve, T. R., Stern, D., Ivison, R. J., De Breuck, C., Kovács, A., & Bertoldi, F. 2007, MNRAS, 382, 48

Griffith, R. L., & Stern, D. 2010, AJ, 140, 533

Haas, M., et al. 2004, A&A, 424, 531

Haas, M., Willner, S. P., Heymann, F., Ashby, M. L. N., Fazio, G. G., Wilkes, B. J., Chini, R., & Siebenmorgen, R. 2008, ApJ, 688, 122

Häring, N., & Rix, H.-W. 2004, ApJ, 604, L89

Hickox, R. C., et al. 2009, ApJ, 696, 891

Houck, J. R. et al. 2004, ApJS, 154, 18

Isobe, T., Feigelson, E. D., & Nelson, P. I. 1986, ApJ, 306, 490

Ivison, R. J., et al. 2004, ApJS, 154, 124

Ivison, R. J., et al. 2008, MNRAS, 390, 1117

Jaffe, W., et al. 2004, Nature, 429, 47

Jarvis, M. J., Rawlings, S., Eales, S., Blundell, K. M., Bunker, A. J., Croft, S., McLure, R. J., & Willott, C. J. 2001, MNRAS, 326, 1585

John, T. L. 1988, A&A, 193, 189

Kapahi, V. K., & Kulkarni, V. K. 1990, AJ, 99, 1397

Kapahi, V. K., Athreya, R. M., van Breugel, W., McCarthy, P. J., & Subrahmanya, C. R. 1998, ApJS, 118, 275

Keel, W. C., Wu, W., Waddington, I., Windhorst, R. A., & Pascarelle, S. M. 2002, AJ, 123, 3041

Kroupa, P. 2001, MNRAS, 322, 231

Kuiper, E., et al. 2010, MNRAS, 512

Lacy, M., Rawlings, S., & Warner, P. J. 1992, MNRAS, 256, 404

Lacy, M., Riley, J. M., Waldram, E. M., McMahon, R. G., & Warner, P. J. 1995, MNRAS, 276, 614

Lacy, M. 1999, The Hy-Redshift Universe: Galaxy Formation and Evolution at High Redshift, 193, 94

Lacy, M., et al. 2004, ApJS, 154, 166

Landt, H., Buchanan, C. L., & Barmby, P. 2010, MNRAS, in press, arXiv:1007.0278

Law-Green, J. D. B., Leahy, J. P., Alexander, P., Allington-Smith, J. R., van Breugel, W. J. M., Eales, S. A., Rawlings, S. G., & Spinrad, H. 1995, MNRAS, 274, 939

Law-Green, J. D. B., Eales, S. A., Leahy, J. P., Rawlings, S., & Lacy, M. 1995, MNRAS, 277, 995

Leipski, C., Antonucci, R., Ogle, P., & Whysong, D. 2009, ApJ, 701, 891
Leipski, C., et al. 2010, ApJ, 717, 766
Lilly, S. J. & Longair, M. S. 1984, MNRAS, 211, 833
Magorrian, J., et al. 1998, AJ, 115, 2285
Matthews, T. A., Morgan, W. W., & Schmidt, M. 1964, ApJ, 140, 35
McCarthy, P. J., Spinrad, H., Dickinson, M., van Breugel, W., Liebert, J., Djorgovski, S., & Eisenhardt, P. 1990, ApJ, 365, 487
McCarthy, P. J., van Breugel, W., Kapahi, V. K., & Subrahmanya, C. R. 1991, AJ, 102, 522
Meisenheimer, K., Haas, M., Müller, S. A. H., Chini, R., Klaas, U., & Lemke, D. 2001, A&A, 372, 719
Miley, G., & De Breuck, C. 2008, A&A Rev., 15, 67
Mor, R., Netzer, H., & Elitzur, M. 2009, ApJ, 705, 298
Napier, P. J., Thompson, A. R., & Ekers, R. D. 1983, IEEE Proceedings, 71, 1295
Nenkova, M., Ivezić, Ž., & Elitzur, M. 2002, ApJ, 570, L9
Nesvadba, N. P. H., et al. 2009, MNRAS, 395, L16
Nesvadba, N., De Breuck, C., Lehnert, M., Best, P., Binette, L., & Proga, D. 2010, A&A, in press
Ogle, P., Whysong, D., & Antonucci, R. 2006, ApJ, 647, 161
Orr, M. J. L., & Browne, I. W. A. 1982, MNRAS, 200, 1067
Overzier, R. A., Harris, D. E., Carilli, C. L., Pentericci, L., Röttgering, H. J. A., & Miley, G. K. 2005, A&A, 433, 87
Park, S. Q., et al. 2010, ApJ, 717, 1181
Pentericci, L., Van Reeven, W., Carilli, C. L., Röttgering, H. J. A., & Miley, G. K. 2000, A&AS, 145, 121
Pentericci, L., McCarthy, P. J., Röttgering, H. J. A., Miley, G. K., van Breugel, W. J. M., & Fosbury, R. 2001, ApJS, 135, 63
Pérez-Torres, M.-A., & De Breuck, C. 2005, MNRAS, 363, L41
Pier, E. A., & Krolik, J. H. 1992, ApJ, 401, 99
Pope, A., et al. 2008, ApJ, 675, 1171
Ramos Almeida, C., Tadhunter, C. N., Inskip, K. J., Morganti, R., Holt, J., & Dicken, D. 2010, arXiv:1008.2683
Rawlings, S., Lacy, M., Blundell, K. M., Eales, S. A., Bunker, A. J., & Garrington, S. T. 1996, Nature, 383, 502
Rengelink, R. B., Tang, Y., de Bruyn, A. G., Miley, G. K., Bremer, M. N., Röttgering, H. J. A., & Bremer, M. A. R. 1997, A&AS, 124, 259
Reuland, M., Röttgering, H., van Breugel, W., & De Breuck, C. 2004, MNRAS, 353, 377
Richards, G. T., et al. 2006, ApJS, 166, 470
Rieke, G. H. et al. 2004, ApJS, 154, 25
Rieke, G. H., Alonso-Herrero, A., Weiner, B. J., Pérez-González, P. G., Blaylock, M., Donley, J. L., & Marcillac, D. 2009, ApJ, 692, 556
Rocca-Volmerange, B., Le Borgne, D., De Breuck, C., Fioc, M., & Moy, E. 2004, A&A, 415, 931
Sawicki, M. 2002, AJ, 124, 3050
Seymour, N., et al. 2007, ApJS, 171, 353
Seymour, N., et al. 2008, ApJ, 681, L1
Shi, Y., et al. 2005, ApJ, 629, 88
Siebenmorgen, R., & Krügel, E. 2007, A&A, 461, 445
Simpson, C., & Eisenhardt, P. 1999, PASP, 111, 691
Simpson, C., & Rawlings, S. 2002, MNRAS, 334, 511
Smith, D. J. B., Simpson, C., Swinbank, A. M., Rawlings, S., & Jarvis, M. J. 2010, MNRAS, in press, arXiv:1001.2018
Spinrad, H., Dey, A., Stern, D., Dunlop, J., Peacock, J., Jimenez, R., & Windhorst, R. 1997, ApJ, 484, 581
Stern, D., et al. 2005, ApJ, 631, 163
Stern, D., Chary, R.-R., Eisenhardt, P. R. M., & Moustakas, L. A. 2006, AJ, 132, 1405
Tananka, I., De Breuck, C, Kurk, J., Taniguchi, Y., Kodama, T., Matsuda, Y. et al. 2010, PASJ, submitted
van Breugel, W. J. M., Stanford, S. A., Spinrad, H., Stern, D., & Graham, J. R. 1998, ApJ, 502, 614
van Ojik, R., Röttgering, H. J. A., Carilli, C. L., Miley, G. K., Bremer, M. N., & Macchetto, F. 1996, A&A, 313, 25
van Ojik, R., Röttgering, H. J. A., Miley, G. K., & Hunstead, R. W. 1997, A&A, 317, 358
Venemans, B. P., et al. 2007, A&A, 461, 823
Vernet, J., Fosbury, R. A. E., Villar-Martín, M., Cohen, M. H., Cimatti, A., di Serego Alighieri, S., & Goodrich, R. W. 2001, A&A, 366, 7
Villar-Martín, M., et al. 2006, MNRAS, 366, L1
Villar-Martín, M., Humphrey, A., De Breuck, C., Fosbury, R., Binette, L., & Vernet, J. 2007, MNRAS, 375, 1299
White, R. L., Becker, R. H., Helfand, D. J., & Gregg, M. D. 1997, ApJ, 475, 479
Willott, C. J., Rawlings, S., Blundell, K. M., & Lacy, M. 1999, MNRAS, 309, 1017
Willott, C. J., Rawlings, S., Jarvis, M. J., & Blundell, K. M. 2003, MNRAS, 339, 173
Zirm, A. W., Dickinson, M., & Dey, A. 2003, ApJ, 585, 90

Table 1
Spitzer HzRG sample and exposure times per instrument.

HzRG	RA[a] (J2000)	Dec.[a] (J2000)	Redshift	K-band[b] (Vega)	IRAC (s)	IRS (s)	MIPS 24, 70, 160 μm (s)
6C 0032+412	00:34:53.09	+41:31:31.5	3.670	19.1	120	122	134, 420, 881
MRC 0037-258	00:39:56.41	−25:34:31.0	1.100	17.1	120	305	267, -, -
6C*0058+495	01:01:18.85	+49:50:12.3	1.173	17.6	120	305	134, 420, 881
MRC 0114-211	01:16:51.44	−20:52:06.7	1.410	18.5	120	305	267, -, -
TN J0121+1320	01:21:42.73	+13:20:58.0	3.516	18.7	120	122	267, -, -
6C*0132+330	01:35:30.37	+33:16:59.6	1.710	18.8	120	305	267, -, -
6C 0140+326	01:43:43.82	+32:53:49.3	4.413	19.9	5000	122	267, 671, 2643
MRC 0152-209	01:54:55.76	−20:40:26.3	1.920	17.9	120	305	534, -, -
MRC 0156-252	01:58:33.44	−24:59:31.7	2.016	16.1	120	122	-, -, -
TN J0205+2242	02:05:10.69	+22:42:50.4	3.506	18.7	120	122	267, -, -
MRC 0211-256	02:13:30.54	−25:25:20.6	1.300	$\cdots$	120	122	267, -, -
TXS 0211-122	02:14:17.40	−11:58:46.0	2.340	17.3	120	305	267, -, -
3C 65	02:23:43.46	+40:00:52.7	1.176	16.8	120	305	267, -, -
MRC 0251-273	02:53:16.68	−27:09:11.6	3.160	18.5	120	122	267, -, -
MRC 0316-257	03:18:12.06	−25:35:09.7	3.130	18.1	46000	122	267, -, -
MRC 0324-228	03:27:04.54	−22:39:42.1	1.894	18.8	120	305	267, -, -
MRC 0350-279	03:52:51.64	−27:49:22.6	1.900	19.0	120	305	134, 420, 881
MRC 0406-244	04:08:51.46	−24:18:16.4	2.427	17.4	120	122	134, 420, 881
4C60.07	05:12:55.15	+60:30:51.0	3.788	19.2	120	122	134, 420, 881
PKS 0529-549	05:30:25.39	−54:54:23.2	2.575	20.0	120	122	134, 420, 881
WN J0617+5012	06:17:39.35	+50:12:54.2	3.153	19.7	120	122	267, -, -
4C41.17	06:50:52.23	+41:30:30.1	3.792	19.1	5000	122	267, 671, 2643
WN J0747+3654	07:47:29.38	+36:54:38.1	2.992	20.0	120	122	267, -, -
6CE 0820+3642	08:23:48.11	+36:32:46.4	1.860	18.2	120	305	267, -, -
5C 7.269	08:28:38.78	+25:28:27.1	2.218	18.9	120	122	267, -, -
USS 0828+193	08:30:53.42	+19:13:15.7	2.572	18.2	120	122	267, -, -
6CE 0901+3551	09:04:32.28	+35:39:04.1	1.910	18.1	120	305	267, -, -
B2 0902+34	09:05:30.14	+34:07:56.0	3.395	19.9	1200	122	2557, 2696, 3556
6CE 0905+3955	09:08:16.90	+39:43:26.0	1.883	18.3	120	305	267, -, -
TN J0924-2201	09:24:19.94	−22:01:42.3	5.195	19.7	120	122	134, 420, 881
6C 0930+389	09:33:06.91	+38:41:50.1	2.395	19.5	120	122	267, -, -
USS 0943-242	09:45:32.73	−24:28:49.7	2.923	19.2	120	122	134, 420, 881
3C 239	10:11:45.42	+46:28:19.8	1.781	17.8	120	305	267, -, -
MG 1019+0534	10:19:33.43	+05:34:34.8	2.765	19.1	120	122	267, -, -
MRC 1017-220	10:19:49.04	−22:19:59.6	1.768	17.4	120	305	267, -, -
WN J1115+5016	11:15:06.87	+50:16:23.9	2.540	19.2	120	122	267, -, -
3C 257	11:23:09.40	+05:30:18.9	2.474	17.8	120	122	267, -, -
WN J1123+3141	11:23:55.74	+31:41:26.7	3.217	17.4	120	122	267, -, -
PKS 1138-262	11:40:48.38	−26:29:08.8	2.156	16.1	3000	122	9000, -, -
3C 266	11:45:43.37	+49:46:08.2	1.275	17.1	120	305	267, -, -
6C 1232+39	12:35:04.75	+39:25:38.9	3.220	18.0	120	122	267, -, -
USS 1243+036	12:45:38.36	+03:23:20.7	3.570	19.2	120	122	267, -, -
TN J1338-1942	13:38:26.09	−19:42:30.7	4.110	19.6	5000	122	267, -, -
4C 24.28	13:48:14.87	+24:15:50.5	2.879	$\cdots$	120	122	267, -, -
3C 294.0	14:06:53.25	+34:11:21.1	1.786	17.9	120	305	267, -, -
USS 1410-001	14:13:15.10	−00:22:59.7	2.363	$\cdots$	120	122	267, -, -
8C 1435+635	14:36:37.21	+63:19:14.4	4.250	19.4	120	122	134, 420, 881
USS 1558-003	16:01:17.30	+00:28:46.2	2.527	$\cdots$	120	122	267, -, -
USS 1707+105	17:10:06.86	+10:31:10.2	2.349	$\cdots$	120	122	267, -, -
LBDS 53W002	17:14:14.79	+50:15:30.6	2.393	18.9	3300	122	134, 420, 881
LBDS 53W091	17:22:32.93	+50:06:01.3	1.552	18.7	900	305	633, 1311, 2643
3C 356.0	17:24:19.33	+50:57:36.2	1.079	16.8	120	305	134, 420, 881
7C 1751+6809	17:50:50.03	+68:08:26.4	1.540	18.2	120	305	134, 420, 881
7C 1756+6520	17:57:05.44	+65:19:53.1	1.416	18.9	120	305	134, 420, 881
3C 368.0	18:05:06.37	+11:01:33.1	1.132	17.2	120	305	134, 420, 881
7C 1805+6332	18:05:56.81	+63:33:13.1	1.840	18.8	120	305	134, 420, 881
4C 40.36	18:10:55.70	+40:45:24.0	2.265	17.8	120	122	134, 420, 881
TXS J1908+7220	19:08:23.70	+72:20:11.8	3.530	16.5	120	122	134, 420, 881
WN J1911+6342	19:11:49.63	+63:42:09.6	3.590	19.9	120	122	134, 420, 881
TN J2007-1316	20:07:53.26	−13:16:43.6	3.840	18.8	120	122	267, -, -
MRC 2025-218	20:27:59.48	−21:40:56.9	2.630	18.5	120	122	267, -, -
MRC 2048-272	20:51:03.59	−27:03:02.5	2.060	18.3	120	122	267, -, -
MRC 2104-242	21:06:58.28	−24:05:09.1	2.491	$\cdots$	120	122	267, -, -
4C 23.56	21:07:14.80	+23:31:45.0	2.483	19.7	120	122	134, 420, 881
MG 2144+1928	21:44:07.56	+19:29:14.6	3.592	19.1	120	122	267, -, -
USS 2202+128	22:05:14.18	+13:05:33.0	2.706	18.4	120	122	267, -, -
MRC 2224-273	22:27:43.26	−27:05:01.7	1.679	18.5	120	305	267, -, -
B3 J2330+3927	23:30:24.82	+39:27:12.5	3.086	18.8	120	122	134, 420, 881
4C 28.58	23:51:59.20	+29:10:29.0	2.891	18.7	120	122	267, -, -
3C 470	23:58:36.00	+44:04:45.0	1.653	18.5	120	305	134, 420, 881

[a] J2000 coordinates of the identification in the bluest IRAC channel.
[b] K-band magnitude within projected 64 kpc radius, taken from S07.

Table 2
Radio data for the SHzRG sample.

HzRG	$\log(L_{500\,\mathrm{MHz}})$ (W Hz^{-1})	$\log(L_{3\,GHz})$ (W Hz^{-1})	Morph[a]	θ^b (arcsec)	CF_{20}^c (%)	Reference
6C 0032+412	28.75	27.75	T	2.3	2.0	Blundell et al. (1998)
MRC 0037-258	27.72	27.07	T	27.6	1.6	this paper; Kapahi et al. (1998)
6C* 0058+495	27.33	26.68	D	3.2	$\cdots$	Blundell et al. (1998)
MRC 0114-211	28.66	28.39	T	0.7	0.3	this paper; Kapahi et al. (1998)
TN J0121+1320	28.49	27.41	D	0.3	$\cdots$	De Breuck et al. (2000)
6C* 0132+330	27.64	26.60	T	2.2	9	this paper
6C 0140+326	28.73	27.89	D	2.5	$\cdots$	Blundell et al. (1998)
MRC 0152-209	28.20	27.77	D	2.2	$\cdots$	Pentericci et al. (2000)
MRC 0156-252	28.46	27.79	T	8.3	10.0	Carilli et al. (1997)
TN J0205+2242	28.46	27.43	D	2.7	$\cdots$	De Breuck et al. (2000)
MRC 0211-256	27.78	26.22	S	<1.5	$\cdots$	Kapahi et al. (1998)
TXS 0211-122	28.48	27.81	T	17.0	3.8	Carilli et al. (1997)
3C 65	28.63	28.06	T	17.5	0.1	Best et al. (1997); Corbin et al. (1998)
MRC 0251-273	28.54	28.09	T	3.9	3.5	this paper; Kapahi et al. (1998)
MRC 0316-257	28.95	28.26	D	6.7	$\cdots$	McCarthy et al. (1991); Athreya et al. (1997)
MRC 0324-228	28.49	27.81	T	9.5	0.2	this paper; McCarthy et al. (1991)
MRC 0350-279	28.25	27.61	D	1.2	$\cdots$	this paper; Kapahi et al. (1998)
MRC 0406-244	29.03	28.11	T	10.0	2.6	Carilli et al. (1997)
4C 60.07	29.20	27.91	T	9.0	2.1	Carilli et al. (1997)
PKS 0529-549	29.16	28.27	D	1.2	<10	Broderick et al. (2007)
WN J0617+5012	28.02	26.97	D	3.4	$\cdots$	De Breuck et al. (2000)
4C 41.17	29.18	28.17	T	20.0	2.4	Carilli et al. (1994)
WN J0747+3654	28.14	27.02	S	2.1	$\cdots$	De Breuck et al. (2000)
6CE 0820+3642	28.28	27.49	T	23.4	0.9	this paper; Law-Green et al. (1995)
5C 7.269	27.82	27.08	D	7.6	$\cdots$	this paper
USS 0828+193	28.44	27.47	T	12.8	21.0	Carilli et al. (1997)
6CE 0901+3551	28.19	27.47	T	2.9	0.4	this paper
B2 0902+34	28.78	28.27	T	4.2	18.0	Carilli et al. (1994)
6CE 0905+3955	28.17	27.49	T	111	0.6	Law-Green et al. (1995)
TN J0924-2201	29.51	27.83	D	1.2	$\cdots$	De Breuck et al. (2000)
6C 0930+389	28.41	27.79	T	4.2	0.8	Pentericci et al. (2000)
USS 0943-242	28.62	27.95	D	3.9	$\cdots$	Carilli et al. (1997)
3C 239	29.00	28.19	T	11.9	0.3	Best et al. (1997)
MG 1019+0534	28.57	28.13	T	2.2	4.7	Pentericci et al. (2000)
MRC 1017-220	27.94	28.11	S	<0.2	$\cdots$	Pentericci et al. (2000)
WN J1115+5016	27.82	26.87	D	0.2	$\cdots$	De Breuck et al. (2000)
3C 257	29.16	28.62	D	12	$\cdots$	van Breugel et al. (1998)
WN J1123+3141	28.51	27.42	T	25.8	5.5	White et al. (1997)
PKS 1138-262	29.07	28.14	T	15.8	3.1	Carilli et al. (1997)
3C 266	28.54	27.80	D	4.6	<0.1	Best et al. (1997)
6C 1232+39	28.93	28.01	T	8.0	0.7	Carilli et al. (1997)
USS1243+036	29.23	28.25	T	6.0	1.7	van Ojik et al. (1996)
TN J1338-1942	28.71	27.90	T	5.2	1.9	Pentericci et al. (2000)
4C 24.28	29.05	28.25	T	2.3	0.7	Carilli et al. (1997)
3C 294.0	28.96	28.12	T	14.5	0.3	McCarthy et al. (1990)
USS 1410-001	28.41	27.69	T	24.0	6.7	Carilli et al. (1997)
8C 1435+635	29.40	28.55	T	4.3	3.3	Carilli et al. (1997)
USS 1558-003	28.82	28.00	T	9.2	1.6	Pentericci et al. (2000)
USS 1707+105	28.63	27.78	D	22.5	$\cdots$	Pentericci et al. (2001)
LBDS 53W002	27.78	27.02	S	<1.5	$\cdots$	Fomalont et al. (2002)
LBDS 53W091	27.04	26.29	D	4.3	$\cdots$	Kapahi & Kulkarni (1990); Spinrad et al. (1997)
3C 356.0	28.35	27.65	T	76.2	0.1	Best et al. (1997)
7C 1751+6809	27.46	27.01	D	2.0	$\cdots$	this paper; Lacy et al. (1992)
7C 1756+6520	27.40	27.00	D	2.7	$\cdots$	this paper; Lacy et al. (1992)
3C 368.0	28.52	27.63	T	8.8	0.2	Best et al. (1997)
7C 1805+6332	27.78	27.12	T	15.6	0.6	this paper; Lacy et al. (1992)
4C 40.36	28.79	27.94	D	4.0	$\cdots$	Carilli et al. (1997)
TXS J1908+7220	29.12	28.15	T	15.4	4.8	Pentericci et al. (2000)
WN J1911+6342	28.14	27.03	S	1.8	$\cdots$	De Breuck et al. (2000)
TN J2007-1316	29.13	27.79	T	3.5	15	this paper
MRC 2025-218	28.74	27.96	T	5.1	0.7	Carilli et al. (1997)
MRC 2048-272	28.72	27.85	D	6.7	<0.2	Pentericci et al. (2000)
MRC 2104-242	28.84	27.88	T	23.7	0.7	Pentericci et al. (2000)
4C 23.56	28.93	28.26	T	53.0	14.6	Carilli et al. (1997)
MG 2144+1928	29.08	28.27	D	8.9	$\cdots$	Carilli et al. (1997)
USS 2202+128	28.54	27.75	T	4.2	0.9	Carilli et al. (1997)
MRC 2224-273	27.52	27.39	S	<0.2	$\cdots$	Pentericci et al. (2000)
B3 J2330+3927	28.33	27.59	T	3.0	50	Pérez-Torres & De Breuck (2005)
4C 28.58	28.91	27.89	T	14.5	2.0	Cai et al. (2002); Chambers et al. (1996)
3C 470	28.79	28.24	T	24.6	0.4	Best et al. (1997)

[a] Radio source morphology: S=Single component, D=Double component, T=Three or more components, including a radio core.
[b] Largest angular size of the radio source; see Carilli et al. (1997).
[c] Core fraction at restframe 20 GHz; see Carilli et al. (1997).

Table 3
Spitzer photometry for HzRGs (μJy).

HzRG	$f_{3.6\mu m}$	$f_{4.5\mu m}$	$f_{5.8\mu m}$	$f_{8.0\mu m}$	$f_{16\mu m}$	$f_{24\mu m}$	$f_{70\mu m}$	$f_{160\mu m}$
6C 0032+412	15.4± 2.1	33.8± 3.7	57.6± 8.9	98.3± 10.0	412± 83	467± 42	< 3950	< 96000
MR C0037-258	221.0±22.0	248.0±25.0	286.0±29.0	518.0± 52.0	877±100	1740± 39	$\cdots$	$\cdots$
6C*0058+495	82.0± 8.3	86.7± 8.8	93.2± 9.5	309.0± 31.0	1280±100	1490± 50	18900±1962	< 94600
MRC 0114-211	87.3± 8.9	117.0±12.0	157.0±16.0	398.0± 40.0	1690±100	2090± 40	$\cdots$	$\cdots$
TN J0121+1320	10.5± 1.8	14.4± 2.1	< 32.5	< 40.3	<204	<131	$\cdots$	$\cdots$
6C* 0132+330	31.6± 3.6	41.3± 4.5	51.9±12.4	109.0± 11.0	<280	109± 25	$\cdots$	$\cdots$
6C 0140+326	< 623.0	< 450.0	< 34.9	<36.3	<160	<2190	< 2580	< 20700
MRC 0152-209	108.0±11.0	165.0±17.0	215.0±22.0	415.0± 42.0	1580±100	3320±133	$\cdots$	$\cdots$
MRC 0156-252	291.0±29.0	405.0±41.0	717.0±72.0	1125.0±113.0	1980±100	$\cdots$	$\cdots$	$\cdots$
TN J0205+2242	7.5± 1.7	4.7± 2.3	< 29.3	< 37.4	<211	<116	$\cdots$	$\cdots$
MRC 0211-256	166.0±17.0	197.0±20.0	222.0±22.0	278.0± 28.0	378± 86	710± 35	$\cdots$	$\cdots$
TXS 0211-122	30.2±0.7	47.4±1.1	126.5±6.3	462.2±7.9	1590±220	2750± 40	$\cdots$	$\cdots$
3C 65	161.0±32.0	$\cdots$	320.0±66.0	$\cdots$	1220±330	2072± 30	$\cdots$	$\cdots$
MRC 0251-273	11.5± 1.6	12.7± 1.8	< 29.1	< 28.8	102± 33	476± 33	$\cdots$	$\cdots$
MRC 0316-257	19.3± 2.1	20.1± 2.1	19.5± 2.4	38.1± 4.1	<156	<102	$\cdots$	$\cdots$
MRC 0324-228	39.4± 4.2	39.7± 4.3	61.1± 8.6	89.9± 9.9	530± 54	1880± 35	$\cdots$	$\cdots$
MRC 0350-279	23.6± 2.6	40.6± 4.2	82.2±27.6	79.3± 26.5	208± 40	306± 44	< 1040	< 88800
MRC 0406-244	40.4± 4.3	43.3± 4.6	< 51.6	63.5± 14.5	637± 86	1540± 40	24700±2306	< 47700
4C60.07	20.6± 3.1	27.0± 2.0	< 26.0	< 39.0	$\cdots$ ^{a}	$\cdots$ ^{a}	< 3750	< 64600
PKS 0529-549	46.6± 4.9	52.9± 5.5	62.7± 8.6	72.2± 9.1	248± 89	966± 40	< 4110	< 74100
WN J0617+5012	3.6± 1.0	5.5± 1.2	< 48.3	< 54.5	<203	<122	$\cdots$	$\cdots$
4C41.17	23.4± 2.4	27.5± 2.8	35.6± 3.7	36.5± 3.5	<181	370± 40	< 3210	< 26300
WN J0747+3654	19.1± 2.4	25.3± 3.0	< 29.9	44.9± 11.5	<198	<117	$\cdots$	$\cdots$
6CE 0820+3642	79.2± 8.1	81.9± 8.4	82.0± 8.4	68.0± 7.0	225± 70	1290± 40	$\cdots$	$\cdots$
5C7.269	41.0± 4.5	49.5± 5.3	57.8± 6.1	< 40.1	<260	$\cdots$	$\cdots$	$\cdots$
USS 0828+193	61.7± 6.9	133.0±13.0	201.0±21.0	687.0± 74.0	1910±130	2880± 40	$\cdots$	$\cdots$
6CE 0901+3551	37.2± 4.1	46.5± 5.0	52.8±10.7	69.8± 12.4	410± 70	1340± 40	$\cdots$	$\cdots$
B2 0902+34	6.4± 0.8	9.9± 1.1	11.0± 2.5	41.3± 2.3	450±100	323± 12	$\cdots$	< 18500
6CE 0905+3955	51.8± 5.4	60.1± 6.2	96.8± 9.8	146.0± 14.0	1440±120	3700± 40	$\cdots$	$\cdots$
TN J0924-2201	11.3± 1.8	11.4± 1.9	< 30.6	< 33.0	<168	<125	< 3330	< 52900
6C 0930+389	30.7± 3.4	32.2± 3.6	37.3± 9.2	< 32.6	<180	530± 43	$\cdots$	$\cdots$
USS 0943-242	21.5± 2.6	28.4± 3.2	< 30.9	25.8± 11.7	170± 48	518± 40	< 3390	< 50900
3C 239	96.4± 9.8	111.0±11.0	130.0±12.0	142.0± 14.0	848± 90	1890± 60	$\cdots$	$\cdots$
MG 1019+0534	25.6± 2.9	19.5± 3.8	< 35.4	< 42.9	220± 70	415± 43	$\cdots$	$\cdots$
MRC 1017-220	119.0±12.0	179.0±18.0	273.0±27.0	360.0± 36.0	740±120	1140± 30	$\cdots$	$\cdots$
WN J1115+5016	7.8± 2.1	9.5± 3.0	< 54.8	< 61.1	<160	<100	$\cdots$	$\cdots$
3C 257	85.0± 8.7	111.0±11.0	194.0±19.0	322.0± 33.0	1280±150	1770±130	$\cdots$	$\cdots$
WN J1123+3141	48.2± 5.0	74.4± 7.6	92.7± 9.4	182.6± 18.4	1160±110	1670± 37	$\cdots$	$\cdots$
PKS 1138-262	318.0±32.0	497.0±50.0	887.0±89.0	1500.0±150.0	3020±100	3890± 20	$\cdots$	$\cdots$
3C 266	67.9± 7.0	73.1± 7.5	45.1± 4.7	102.6± 10.4	660±120	985± 22	$\cdots$	$\cdots$
6C 1232+39	33.3± 3.6	41.8± 4.4	52.0± 9.2	75.2± 10.8	360± 80	459± 33	$\cdots$	$\cdots$
USS 1243+036	22.0± 2.5	21.5± 3.0	< 48.0	< 62.9	<260	511± 43	$\cdots$	$\cdots$
TN J1338-1942	17.8± 1.9	10.7± 1.2	14.3± 2.8	9.9± 3.4	<226	<99	$\cdots$	$\cdots$
4C 24.28	16.5± 2.2	27.3± 3.1	43.3± 8.3	102.0± 10.0	573± 96	1140± 40	$\cdots$	$\cdots$
3C 294.0	< 93.0	< 103.0	68.0±16.8	66.6± 20.6	430± 99	471± 31	$\cdots$	$\cdots$
USS 1410-001	50.6± 5.3	79.0± 8.1	166.0±17.0	240.0± 24.0	660±120	1070± 40	$\cdots$	$\cdots$
8C 1435+635	18.6± 2.1	14.7± 2.9	< 45.5	< 50.3	<86	<119	< 4130	< 33900
USS 1558-003	78.8± 8.1	101.0±10.3	105.0±10.5	233.0± 23.4	993±100	1270± 37	$\cdots$	$\cdots$
USS 1707+105	22.1± 2.7	30.1± 3.4	22.6± 9.1	< 33.3	<123	264± 32	$\cdots$	$\cdots$
LBDS 53W002	32.0± 3.3	44.0± 4.5	49.9± 5.2	103.0± 11.0	593±114	648± 40	< 4300	< 65100
LBDS 53W091	43.3± 6.3	51.4± 5.3	23.9± 6.1	26.6± 6.4	<166	<45	< 1610	< 23900
3C 356a	108.0±11.0	110.0±11.0	122.0±14.0	434.0± 47.0	2280±220	4170± 40	< 4400	< 70200
7C 1751+6809	46.6± 4.9	50.8± 5.3	< 40.9	36.5± 16.0	147± 57	342± 34	< 3600	< 51600
7C 1756+6520	39.6± 4.2	46.9± 5.0	34.7± 7.7	42.6± 8.6	220^{a}±114	95^{a}±40	< 5900	< 151000
3C 368.0	126.0±13.0	112.0±11.0	112.0±11.0	210.0± 21.0	1620±180	3350± 50	28800±2710	< 39000
7C 1805+6332	28.4± 3.6	42.1± 4.4	51.4± 5.4	95.6± 17.1	310± 80	673± 35	< 4330	< 111000
4C 40.36	36.5± 3.9	41.3± 4.3	45.4±12.9	26.3± 10.3	54± 28	536± 37	< 4750	< 64500
TXS J1908+7220	200.0±20.0	229.0±23.0	241.0±25.0	480.0± 48.0	1410±170	1910± 49	16200±1905	< 63300
WN J1911+6342	9.5± 1.8	8.7± 1.8	< 26.4	< 26.0	<137	<102	< 3710	< 57100
TN J2007-1316	56.2± 5.9	54.4± 5.8	41.1±10.7	121.3± 12.3	378±113	385± 40	$\cdots$	$\cdots$
MRC 2025-218	68.4± 7.1	77.1± 8.0	86.8±10.9	126.8± 12.9	200± 62	216± 43	$\cdots$	$\cdots$
MRC 2048-272	59.5± 6.2	72.6± 7.5	78.3±10.4	38.4± 13.1	<220	$\cdots$ ^{a}	$\cdots$	$\cdots$
MRC 2104-242	28.1± 3.3	29.7± 3.5	32.8±10.0	< 36.3	<217	709± 48	$\cdots$	$\cdots$
4C 23.56	61.1± 6.4	86.2± 8.8	126.9±12.8	423.7± 42.5	2400± 90	4630± 40	30300±2958	< 70500
MG 2144+1928	22.1± 2.7	18.3± 2.4	< 25.5	< 30.3	<244	529± 33	$\cdots$	$\cdots$
USS 2202+128	60.4± 6.3	95.8± 9.8	120.1±12.1	106.6± 10.8	417± 88	1341± 35	$\cdots$	$\cdots$
MRC 2224-273	61.6± 6.4	86.1± 8.8	98.4±10.0	203.9± 20.5	625±117	1060± 40	$\cdots$	$\cdots$
B3 J2330+3927	99.6±10.1	143.0±14.0	160.0±16.0	474.0± 47.0	1170± 90	2320± 40	< 4670	< 64300
4C 28.58	31.6± 3.5	36.0± 3.9	< 41.7	40.9± 4.4	430± 85	866±155	$\cdots$	$\cdots$
3C 470	49.5±10.4	75.2±11.8	70.9±10.4	266.0± 30.0	1540±180	2750± 40	< 5570	< 102000

^{a} Contaminated by nearby object.

Table 4
Results of SED fitting.

Source	$\log(L_{1.6\,\mu m}/L_\odot)$	$\log(L_{3\,\mu m}/L_\odot)$	$\log(L_{5\,\mu m}/L_\odot)$	$f_{\rm stel}^a$	$\log(L_{\rm H,*}/L_\odot)$	$\log(M_*/M_\odot)$
6C 0032+412	12.07	12.28	12.29	0.21	<11.37	<11.18
MRC 0037-258	11.49	11.50	11.53	0.95	11.44	11.56
6C* 0058+495	11.19	11.20	11.53	0.99	11.16	11.26
MRC 0114-211	11.40	11.70	11.96	0.96	11.36	11.39
TN J0121+1320	11.55	11.36	11.73	0.46	11.19	11.02
6C* 0132+330	11.14	11.33	11.23	0.84	<11.04	<11.03
6C 0140+326	11.84	12.61	12.89	0.88	<11.76	<11.42
MRC 0152-209	11.88	12.15	12.26	0.91	11.80	11.76
MRC 0156-252	12.40	12.57	12.43	0.54	12.11	12.05
TN J0205+2242	11.03	11.42	11.79	0.97	10.99	10.82
MRC 0211-256	11.58	11.49	11.24	0.83	<11.47	<11.54
TXS 0211-122	11.80	12.43	12.40	0.31	<11.26	<11.16
3C 65	11.43	11.66	11.73	0.92	<11.37	<11.47
MRC 0251-273	11.33	11.57	11.88	0.66	11.12	10.96
MRC 0316-257	11.49	11.77	11.70	0.79	11.37	11.20
MRC 0324-228	11.33	11.44	11.71	0.96	11.29	11.25
MRC 0350-279	11.24	11.44	11.30	0.69	<11.04	<11.00
MRC 0406-244	11.53	11.65	12.10	0.99	11.49	11.38
4C 60.07	11.73	12.51	12.91	0.88	11.65	11.44
PKS 0529-549	11.66	11.75	11.95	0.94	11.60	11.46
WN J0617+5012	11.18	11.38	11.49	0.37	10.72	10.55
4C 41.17	11.66	12.00	12.21	0.93	11.60	11.39
WN J0747+3654	11.55	11.43	11.38	0.63	11.33	11.15
6CE 0820+3642	11.57	11.19	11.27	0.95	11.52	11.48
5C 7.269	11.51	11.06	11.89	0.95	11.46	11.38
USS 0828+193	12.18	12.75	12.68	0.40	<11.75	<11.60
6CE 0901+3551	11.34	11.37	11.61	0.97	11.30	11.25
B2 0902+34	11.52	12.15	12.06	0.30	<10.97	<10.81
6CE 0905+3955	11.47	11.73	12.16	0.98	11.43	11.39
TN J0924-2201	12.19	12.40	12.18	0.21	11.50	11.10
6C 0930+389	11.32	11.44	11.80	0.99	11.28	11.17
USS 0943-242	11.43	11.49	11.93	0.99	11.40	11.22
3C 239	11.66	11.57	11.90	0.99	11.63	11.60
MG 1019+0534	11.36	11.53	11.89	0.99	11.32	11.15
MRC 1017-220	11.84	11.97	11.85	0.81	<11.72	<11.70
WN J1115+5016	10.95	11.48	11.55	0.82	10.84	10.70
3C 257	12.03	12.42	12.44	0.81	<11.91	<11.78
WN J1123+3141	12.13	12.67	12.68	0.60	<11.89	<11.72
PKS 1138-262	12.52	12.84	12.73	0.68	<12.33	<12.26
3C 266	11.13	10.90	11.10	0.99	11.10	11.18
6C 1232+39	11.80	12.18	12.15	0.73	<11.64	<11.47
USS 1243+036	11.62	12.17	12.28	0.71	<11.45	<11.27
TN J1338-1942	11.37	11.55	11.92	0.99	11.34	11.04
4C 24.28	11.58	12.18	12.27	0.53	<11.28	<11.11
3C 294.0	11.41	11.29	11.56	0.99	11.38	11.36
USS 1410-001	11.92	12.02	11.86	0.42	<11.52	<11.41
8C 1435+635	11.80	12.04	12.08	0.56	11.53	11.21
USS 1558-003	11.95	12.05	12.05	0.82	<11.83	<11.70
USS 1707+105	11.29	10.86	10.96	0.89	11.21	11.11
LBDS 53w002	11.55	11.72	11.68	0.71	<11.38	<11.27
LBDS 53w091	11.20	10.59	10.20	1.00	11.18	11.19
3C 356.0	11.21	11.23	11.62	0.99	11.18	11.29
7C 1751+6809	11.20	10.78	10.91	1.00	11.17	11.19
7C 1756+6520	11.15	10.92	11.32	1.00	11.12	11.15
3C 368.0	11.35	11.10	11.41	1.00	11.32	11.43
7C 1805+6332	11.21	11.39	11.40	0.84	<11.11	<11.07
4C 40.36	11.43	10.93	11.14	0.95	11.38	11.29
TX J1908+7220	12.70	12.91	12.82	0.59	<12.44	<12.27
WN J1911+6342	11.38	11.94	11.87	0.57	11.11	10.93
TN J2007-1316	12.19	12.42	12.24	0.56	<11.92	<11.69
MRC 2025-218	11.87	11.86	11.69	0.87	<11.78	<11.62
MRC 2048-272	11.56	11.30	11.68	1.00	11.53	11.47
MRC 2104-242	11.35	11.55	11.94	0.98	11.32	11.19
4C 23.56	11.89	12.60	12.74	0.71	<11.71	<11.59
MG 2144+1928	11.49	12.22	12.32	0.70	<11.31	<11.13
USS 2202+128	11.97	11.61	11.89	0.70	11.78	11.62
MRC 2224-273	11.47	11.63	11.78	0.95	11.42	11.41
B3 J2330+3927	12.43	12.71	12.66	0.51	<12.11	<11.94
4C 28.58	11.57	11.84	12.24	0.98	11.54	11.36
3C 470	11.35	11.72	12.02	0.95	11.30	11.30

^{a} Stellar fraction at $1.6\,\mu m$ in our SED model (see §3.2).

Table 5
Binary AGNs

Source	RA (J2000)	Dec. (J2000)	$f_{3.6\,\mu m}$ (μJy)	$f_{4.5\,\mu m}$ (μJy)	$f_{5.8\,\mu m}$ (μJy)	$f_{8.0\,\mu m}$ (μJy)	$f_{16\,\mu m}$ (μJy)	$f_{24\,\mu m}$ (μJy)
4C 60.07B	05 12 54.76	+60 30 48.9	<3.3	7.8±1.0	23.5±3.3	43.3± 5.1	555± 83	1390±50
3C 356b	17 24 19.02	+50 57 40.3	72.6±7.3	71.1±7.2	69.4±7.5	231.9±23.4	2280±220	4170±40
Cl 1756.7	17 57 04.98	+65 19 51.0	23.0±2.3	33.7±3.4	28.1±3.8	37.6± 4.7	220±150	370±40
MRC 2048−272B	20 51 03.30	−27 03 03.2	24.6±2.5	32.9±3.4	35.2±4.7	34.3± 5.0	<220	491±42